

LEIDEN UNIVERSITY

BACHELOR PROJECT

---

# Sparse Aperture Masking at the Leiden Old Observatory

---

*Author:*

Emiel Por

[por@strw.leidenuniv.nl](mailto:por@strw.leidenuniv.nl)

*Supervisors:*

Dr. Matthew Kenworthy

Dr. Martin van Exter

## Abstract

We designed and implemented a Michelson interferometry observing mode called Sparse Aperture Masking (SAM) or Non-Redundant Masking (NRM) at optical wavelengths on the student telescope located in the Westkoepel in the Leiden Old Observatory. The telescope was transformed into a seven-element interferometer using an aperture mask located in front of the primary mirror. Methods for designing this mask are discussed. A data-reduction pipeline was written in Python and the whole setup was validated using first-light observations of a 3 magnitude contrast binary at  $1.5 \lambda/D$  separation. Algorithms for creating Kolmogorov phase screens involved in simulations are also discussed.

## Contents

<b>1</b>	<b>Introduction</b>	<b>3</b>
<b>2</b>	<b>Non-Redundant Masking (NRM) and fitting theory</b>	<b>4</b>
2.1	Imaging with a baseline . . . . .	4
2.2	Closure phases . . . . .	6
2.3	Binary visibilities . . . . .	7
2.4	Fringe fitting . . . . .	8
2.5	Averaging closure phases . . . . .	11
2.6	Binary parameter estimation . . . . .	13
<b>3</b>	<b>Mask Design</b>	<b>15</b>
3.1	Introduction . . . . .	15
3.2	Requirements and criteria . . . . .	15
3.3	Algorithms . . . . .	16
3.4	Results . . . . .	19
3.5	Possible improvements . . . . .	20
<b>4</b>	<b>Modeling and simulating seeing</b>	<b>24</b>
4.1	Introduction . . . . .	24
4.2	Kolmogorov theory . . . . .	24
4.3	Conventional approach . . . . .	25
4.4	Our method . . . . .	27
4.5	Time dependence . . . . .	30
4.6	Normalisation . . . . .	31
<b>5</b>	<b>Implementation at Leiden Observatory</b>	<b>33</b>
5.1	Student telescope . . . . .	33
5.2	Field expander and filters . . . . .	33

5.3	Mask and mask holder . . . . .	34
5.4	Target choice . . . . .	35
5.5	Observations . . . . .	36
<b>6</b>	<b>Data Reduction</b>	<b>38</b>
6.1	Quick data-reduction . . . . .	38
6.2	Existing pipelines . . . . .	38
6.3	Pre-reduction . . . . .	40
6.4	Mask orientation and pixel scale . . . . .	41
6.5	Star centering . . . . .	42
6.6	Fringe fitting . . . . .	42
6.7	Bispectrum and lucky imaging . . . . .	43
6.8	Binary parameter estimation . . . . .	49
<b>7</b>	<b>Conclusion and future work</b>	<b>53</b>
7.1	Conclusion . . . . .	53
7.2	Future work . . . . .	53
<b>8</b>	<b>Outlook</b>	<b>54</b>
	<b>References</b>	<b>56</b>
<b>A</b>	<b>SAM Observing Guide</b>	<b>60</b>
A.1	Pre-observing . . . . .	60
A.2	During observing . . . . .	61
A.3	Post-observing . . . . .	61
<b>B</b>	<b>SAML Pipeline Manual</b>	<b>61</b>

## 1. Introduction

In a perfect imaging system a point source, such as a star, still has a non-zero width. The star looks like an Airy disk with a width given by the Rayleigh limit  $1.22\lambda/D$ , where  $\lambda$  is the wavelength of the light and  $D$  the diameter of the aperture. This means that we can't observe two stars separately if they are located within this limit. When imaging from the ground, atmosphere turbulence alters the phase of the light over the aperture and therefore creates multiple images of the star, which change rapidly over time. These speckles limit the angular resolution of the telescope to  $\sim \lambda/r_0$ , where  $r_0$  is the Fried parameter, a characteristic length scale for atmospheric seeing, typically  $\sim 15$  cm at a good astronomical site and  $\sim 3$  cm at Leiden.

Several methods exist to overcome the problem of atmospheric seeing. One of the most important ones is *Adaptive Optics* (AO). This method tracks the seeing in the atmosphere and actively corrects for it using a deformable mirror. With this method we can recover diffraction limited images.

Another method, which is the subject of this thesis, is *Sparse Aperture Masking* (SAM). This method doesn't actively correct for the atmosphere, but uses an aperture mask in front of the primary mirror of the telescope, or equivalently in the reimaged pupil plane, to create an optical interferometer. With this interferometer we are able to measure certain astronomical observables that are invariant to the phase shift introduced by the atmosphere. These observables can then be fitted to a model of our science object, or transformed into an image directly.

A subtechnique of SAM is *Non-Redundant Masking* (NRM). This method explicitly uses a mask with holes, of which each baseline (the position of one hole with respect to another) only exists on the mask once, making the mask non-redundant. The light for each pair of holes in the mask interferes in the focal plane, similar to a Youngs Double Slit Experiment, creating an interference fringe. The atmosphere alters the phase of the light at each hole independently, resulting in a phase shift in the created fringe, which changes quickly in time. NRM then analyses these changing phases and combines them into an observable which is invariant with respect to the phase of the light at each hole. This observable is called the closure phase and is a combination of three interference phase shifts. These closure phases are sensitive to source asymmetry, and are therefore very suited for observing binary stars. Contrary to intuition, throwing away as much as 90% of the light actually increases the signal-to-noise-ratio (SNR) significantly if the star is bright enough.

Binary stars are not the only science objects that can be observed using this technique. In the early days of SAM geometrically complex dust envelopes around evolved stars were imaged (Tuthill et al. 2000). More recently SAM observed pre-transitional disks with a possible stellar or substellar companion located within the gap of this disk (Kraus and Ireland 2012; Cieza et al. 2013). In the future, high contrast measurements of similar systems could reveal giant planetary birth (Ireland 2012).

Highly recommended as an introduction to NRM and SAM is a paper by Lacour et al. (2011b),

which describes the capabilities of SAM as established on the VLT with the NAOS-CONICA instrument, directed at potential SAM users. Another nice read is the paper by [Tuthill \(2012\)](#), which describes the history, and present and future developments of SAM.

In this Bachelor thesis we give a short introduction to the theory of NRM and the statistical methods that we use in Section 2. In Section 3 we will design our mask according to NRM requirements and existing algorithms. In Section 4 we will look closer at the statistics of the phase differences of the atmosphere and create a simulation of atmospheric seeing using a new algorithm that improves in simplicity and performance over conventional methods. In Section 5 we describe the implementation of NRM at the Leiden Old Observatory and the first-light observations of a binary star. In Section 6 we describe the pipeline we made to reduce the data and the results of the first-light observations. We describe our conclusions in Section 7 and we show the current research topics of this technique in Section 8.

## 2. Non-Redundant Masking (NRM) and fitting theory

There are many good explanations in literature concerning non-redundant masking and closure phases, such as [Bernat \(2012\)](#) and [Monnier \(2007\)](#). Therefore, in Subsections 2.1 to 2.3 we only give a short summary to the concepts of non-redundant masking, visibilities and closure phases. In Subsections 2.4 to 2.6 we give a summary of the statistical methods used to reduce the data. These include Linear Least Squares (LLS), Maximum Likelihood Estimation (MLE), Non-Linear Least Squares (NLLS), and hypothesis testing.

### 2.1. Imaging with a baseline

We consider a mask consisting of two circular sub-apertures with diameter  $d_{\text{sub}}$ , separated by a distance  $\mathbf{b}$ . A telescope with such a mask can be considered as a Young’s Double Slit Experiment: the light coming through one sub-aperture interferes with the light from the other sub-aperture, forming a sinusoidal fringe oriented in the direction of the sub-aperture separation. We can write the point spread function  $\tau(\boldsymbol{\theta})$  of the mask  $M(\mathbf{r})$ :

$$M(\mathbf{r}) = \Pi(\mathbf{r}) \otimes [\delta(\mathbf{r} - \mathbf{b}/2) + \delta(\mathbf{r} + \mathbf{b}/2)], \quad (1)$$

as

$$\tau(\boldsymbol{\theta}) = \text{Airy}(\pi\boldsymbol{\theta}d_{\text{sub}}/\lambda) [1 + \cos(2\pi\boldsymbol{\theta} \cdot \mathbf{b}/\lambda)], \quad (2)$$

where  $\otimes$  denotes convolution,  $\text{Airy}(\mathbf{x}) = (2J_1(|\mathbf{x}|)/|\mathbf{x}|)^2$  is the Airy disk function,  $J_1(x)$  the Bessel function of the first kind of order one, and  $\Pi(\mathbf{x})$  is given by:

$$\Pi(\mathbf{x}) = \begin{cases} 1 & \text{if } |\mathbf{x}| < \frac{d_{\text{sub}}}{2} \\ 0 & \text{otherwise} \end{cases}. \quad (3)$$

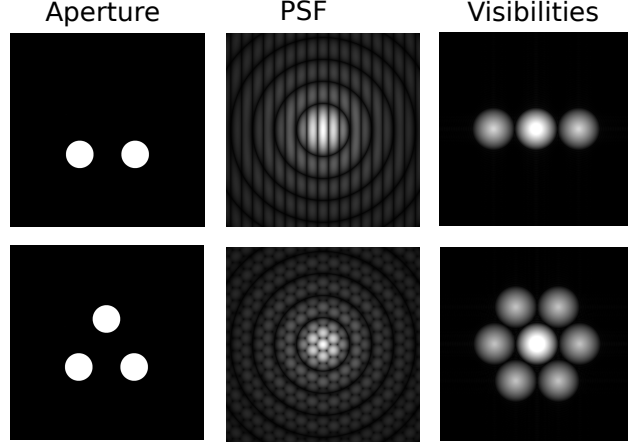


Fig. 1.— The aperture (left), PSF (middle) and visibility plane (right) for a two-aperture mask (top row) and three-aperture mask (bottom row). We can see 3 splodges for a two-aperture mask and 7 for the three-aperture mask.

We can also look at the Fourier transform  $V(\mathbf{f})$  of this point spread function:

$$V(\mathbf{f}) = [(\Pi \star \Pi)(\mathbf{r})]^{\frac{1}{2}} \otimes [\delta(\mathbf{f} - \mathbf{b}/\lambda) + 2\delta(\mathbf{f}) + \delta(\mathbf{f} + \mathbf{b}/\lambda)], \quad (4)$$

where  $\star$  denotes cross-correlation. We can see that  $V(\mathbf{f})$  consists of three spots. The middle spot is the DC Fourier component, proportional to the square of the total flux in the image. The two spots on the side are called *splodges* and these show the baseline of the mask. Note that in this case  $V(\mathbf{f})$  is positive and real everywhere, so that its complex phase is zero. In interferometry we call  $V(\mathbf{f})$  the *visibility*. In Figure 1 we can see the three spots for a two-aperture mask, as well as the same procedure for a three-aperture mask. Each pair of holes in a mask generates two spots, which gives us in total  $n(n - 1) + 1$  spots in the visibility plane for an  $n$ -aperture mask.

When we image an object through this mask, the resulting image  $I(\boldsymbol{\theta})$  is given by the convolution of the intensity function  $O(\boldsymbol{\theta})$  of this object with our point spread function:

$$I(\boldsymbol{\theta}) = \tau(\boldsymbol{\theta}) \otimes O(\boldsymbol{\theta}). \quad (5)$$

In the Fourier transform  $\tilde{I}(\mathbf{f})$  of this image, this convolution becomes a multiplication:

$$\tilde{I}(\mathbf{f}) = V(\mathbf{f}) \tilde{O}(\mathbf{f}), \quad (6)$$

where  $\tilde{O}(\mathbf{f})$  is the Fourier transform of the object intensity function. Note that now the phase can be non-zero as it follows the phase of  $\tilde{O}(\mathbf{f})$ . When we use a mask we therefore sample the source visibility at the baselines given by the mask.

When the light travels through the atmosphere, its phase is altered, both spatially and temporally. In section 4 we will see that the atmosphere introduces phase shifts at each sub-aperture

that are uncorrelated between sub-apertures. This phase shift varies with a characteristic time  $\tau_0$ , which is typically a few milliseconds, so when we take an exposure shorter than this time, the phase shift at each sub-aperture is stationary.

Considering the same, two-aperture mask as before, but with a relative phase shift  $\Delta\phi$  between the holes, we can write the mask  $\hat{M}(\mathbf{r})$  and the point spread function  $\hat{\tau}(\boldsymbol{\theta})$  of this situation as follows:

$$\hat{M}(\mathbf{r}) = \Pi(\mathbf{r}) \otimes \left[ \delta(\mathbf{r} - \mathbf{b}/2) + e^{i\Delta\phi} \delta(\mathbf{r} + \mathbf{b}/2) \right] \quad (7)$$

$$\hat{\tau}(\boldsymbol{\theta}) = \text{Airy}(\pi\boldsymbol{\theta}d_{\text{sub}}/\lambda) [1 + \cos(2\pi\boldsymbol{\theta} \cdot \mathbf{b}/\lambda + \Delta\phi)]. \quad (8)$$

We can see that the relative phase shift directly translates to the phase shift of the interference fringe. This gives for the visibility:

$$\hat{V}(\mathbf{f}) = [\Pi \star \Pi]^{\frac{1}{2}} \otimes [e^{-i\Delta\phi} \delta(\mathbf{f} - \mathbf{b}/\lambda) + 2\delta(\mathbf{f}) + e^{i\Delta\phi} \delta(\mathbf{f} + \mathbf{b}/\lambda)]. \quad (9)$$

We can see that the visibility is now a complex number with a non-zero phase. As this relative phase shift has a variance larger than  $2\pi$ , we can't retrieve the baseline phase of the object because the atmosphere distorts this phase too severely. We therefore have to look at other observables, which are invariant to these relative phase shifts.

## 2.2. Closure phases

One such observable is the closure phase, introduced by [Jennison \(1958\)](#) for radio astronomy. This observable uses three sub-apertures to reach invariance to phase shifts at each hole. For each of the three baselines, the measured visibility is:

$$V_{ij}^{\text{meas}} = G_i G_j^* V_{ij}^{\text{true}} = |G_i||G_j| \exp(i(\phi_i - \phi_j)) V_{ij}^{\text{true}}; \quad (10)$$

$$V_{jk}^{\text{meas}} = G_j G_k^* V_{jk}^{\text{true}} = |G_j||G_k| \exp(i(\phi_j - \phi_k)) V_{jk}^{\text{true}}; \quad (11)$$

$$V_{ki}^{\text{meas}} = G_k G_i^* V_{ki}^{\text{true}} = |G_k||G_i| \exp(i(\phi_k - \phi_i)) V_{ki}^{\text{true}}, \quad (12)$$

where  $G_i$  is the complex gain of sub-aperture  $i$ ,  $\phi_i$  is the phase shift at subaperture  $i$ ,  $V_{ij}^{\text{meas}}$  is the measured visibility of the baseline between subapertures  $i$  and  $j$ , and  $V_{ij}^{\text{true}}$  is the true visibility of the same baseline. The bispectrum is defined as the multiplication of these visibilities:

$$B_{ijk} = V_{ij}^{\text{meas}} V_{jk}^{\text{meas}} V_{ki}^{\text{meas}} \quad (13)$$

$$= |G_i|^2 |G_j|^2 |G_k|^2 V_{ij}^{\text{true}} V_{jk}^{\text{true}} V_{ki}^{\text{true}}. \quad (14)$$

Note that this bispectrum is invariant with respect to the phases of the visibilities, but not with respect to the amplitude gain of these visibilities. The closure phase is defined as the argument of the bispectrum:

$$\phi_{ijk} = \arg B_{ijk} \quad (15)$$

$$= \arg V_{ij}^{\text{true}} + \arg V_{jk}^{\text{true}} + \arg V_{ki}^{\text{true}} \quad (16)$$

Number of sub-apertures	Number of Fourier phases	Number of closing triangles	Number of independent closure phases
3	3	1	1
6	15	20	10
7	21	35	15
9	36	84	28

Table 1: The number of fringes, closure phases and independent closure phases for a varying number of sub-apertures.

For a mask with  $n$  sub-apertures, we have  $n(n - 1)/2$  measured visibilities and we can make  $n(n - 1)(n - 2)/3!$  closure phases. In Table 1 we can see these values for a varying number of sub-apertures. We can see that the closure phases are not linearly independent as there are more closure triangles than Fourier phases. The number of independent closure phases is  $(n - 1)(n - 2)/2$ , which can be shown using counting arguments. This number is lower than the number of Fourier phases, so we lose a lot of visibility sampling if we go from closure phases to visibility phases. We also have to correct for the sparse sampling of the visibility plane. Easing this transformation includes further assumptions such as positive valued image with finite extent. The CLEAN algorithm (Högbom 1974) and the Maximum Entropy Method (Frieden and Swindell 1976; Skilling and Bryan 1984) deal with this reversed procedure. We will not be implementing these procedures.

### 2.3. Binary visibilities

When observing simple targets that can be parametrized by a few parameters, we can estimate these parameters by fitting the theoretical closure phases directly to the observed closure phases. Before considering a binary star, we first calculate the closure phases for a single star. As a model of a single star, we use:

$$O_{\text{single}}(\boldsymbol{\theta}) = \delta(\boldsymbol{\theta} - \boldsymbol{\alpha}), \quad (17)$$

where  $\boldsymbol{\alpha}$  is the off-axis position of the star on the sky, measured as a 2D vector of angles. The closure phases are invariant to this off-axis position, but the visibilities are not. The visibility of this object is the Fourier transform of the object intensity function:

$$V_{\text{single}}(\mathbf{b}) = \exp(i\pi\mathbf{b} \cdot \boldsymbol{\alpha}/\lambda); \quad (18)$$

$$|V_{\text{single}}| = 1; \quad (19)$$

$$\arg(V_{\text{single}}) = \pi\mathbf{b} \cdot \boldsymbol{\alpha}/\lambda. \quad (20)$$

We use for our closure triangle the three baselines  $\mathbf{b}_1$ ,  $\mathbf{b}_2$  and  $\mathbf{b}_3 = -\mathbf{b}_1 - \mathbf{b}_2$ . For the bispectrum and closure phase follows:

$$B_{\text{single}}(\mathbf{b}_1, \mathbf{b}_2) = 1; \quad (21)$$

$$\arg(B_{\text{single}}(\mathbf{b}_1, \mathbf{b}_2)) = 0. \quad (22)$$

We do the same thing for the binary star, consisting of a primary (brightest) star and the secondary (dimmest) star. We use two parameters:  $\rho$  the separation and orientation of the secondary star with respect to the primary, and  $r(\lambda) < 1$  the wavelength dependent contrast ratio between the two stars. The object intensity function and visibility are:

$$O_{\text{binary}}(\boldsymbol{\theta}) = \delta(\boldsymbol{\theta} + \boldsymbol{\rho}/2 - \boldsymbol{\alpha}) + r\delta(\boldsymbol{\theta} - \boldsymbol{\rho}/2 - \boldsymbol{\alpha}); \quad (23)$$

$$V_{\text{binary}}(\mathbf{b}) = \exp(i\pi\mathbf{b} \cdot \boldsymbol{\alpha}/\lambda) \frac{\exp(i\pi\mathbf{b} \cdot \boldsymbol{\rho}/\lambda) + r \exp(-i\pi\mathbf{b} \cdot \boldsymbol{\rho}/\lambda)}{1+r}; \quad (24)$$

$$|V_{\text{binary}}(\mathbf{b})| = \frac{1+r^2+2r\cos(2\pi\mathbf{b} \cdot \boldsymbol{\rho}/\lambda)}{1+r}; \quad (25)$$

$$\arg(V_{\text{binary}}(\mathbf{b})) = \pi\mathbf{b} \cdot \boldsymbol{\alpha}/\lambda + \arctan\left[\frac{r\sin(2\pi\mathbf{b} \cdot \boldsymbol{\rho}/\lambda)}{1+r\cos(2\pi\mathbf{b} \cdot \boldsymbol{\rho}/\lambda)}\right]. \quad (26)$$

Note that the visibility phase is insensitive to binaries with a separation perpendicular with respect to the baseline of the visibility. This means that if we don't know the position angle of the binary, we need a mask that *uniformly* samples all baseline directions and lengths. For the closure phase follows, using the same baseline convention as before:

$$\begin{aligned} \arg(B_{\text{binary}}(\mathbf{b}_1, \mathbf{b}_2)) = & \arctan\left[\frac{r\sin(2\pi\mathbf{b}_1 \cdot \boldsymbol{\rho}/\lambda)}{1+r\cos(2\pi\mathbf{b}_1 \cdot \boldsymbol{\rho}/\lambda)}\right] \\ & + \arctan\left[\frac{r\sin(2\pi\mathbf{b}_2 \cdot \boldsymbol{\rho}/\lambda)}{1+r\cos(2\pi\mathbf{b}_2 \cdot \boldsymbol{\rho}/\lambda)}\right] \\ & - \arctan\left[\frac{r\sin(2\pi(\mathbf{b}_1 + \mathbf{b}_2) \cdot \boldsymbol{\rho}/\lambda)}{1+r\cos(2\pi(\mathbf{b}_1 + \mathbf{b}_2) \cdot \boldsymbol{\rho}/\lambda)}\right]. \end{aligned} \quad (27)$$

The visibilities are plotted for some qualitatively different binaries in Figures 2 and 3.

## 2.4. Fringe fitting

As we use linear least squares (LLS) for fitting the fringes to our data and we extract our fit-errors using the same method, we give a comprehensive summary of the linear least squares algorithm. Let the measured fringes be given by  $\mathbf{y} = (y_1, y_2, \dots, y_m)^\top$ :

$$y_i = \sum_{j=1}^n X_{ij}\beta_j + \epsilon_i \quad (28)$$

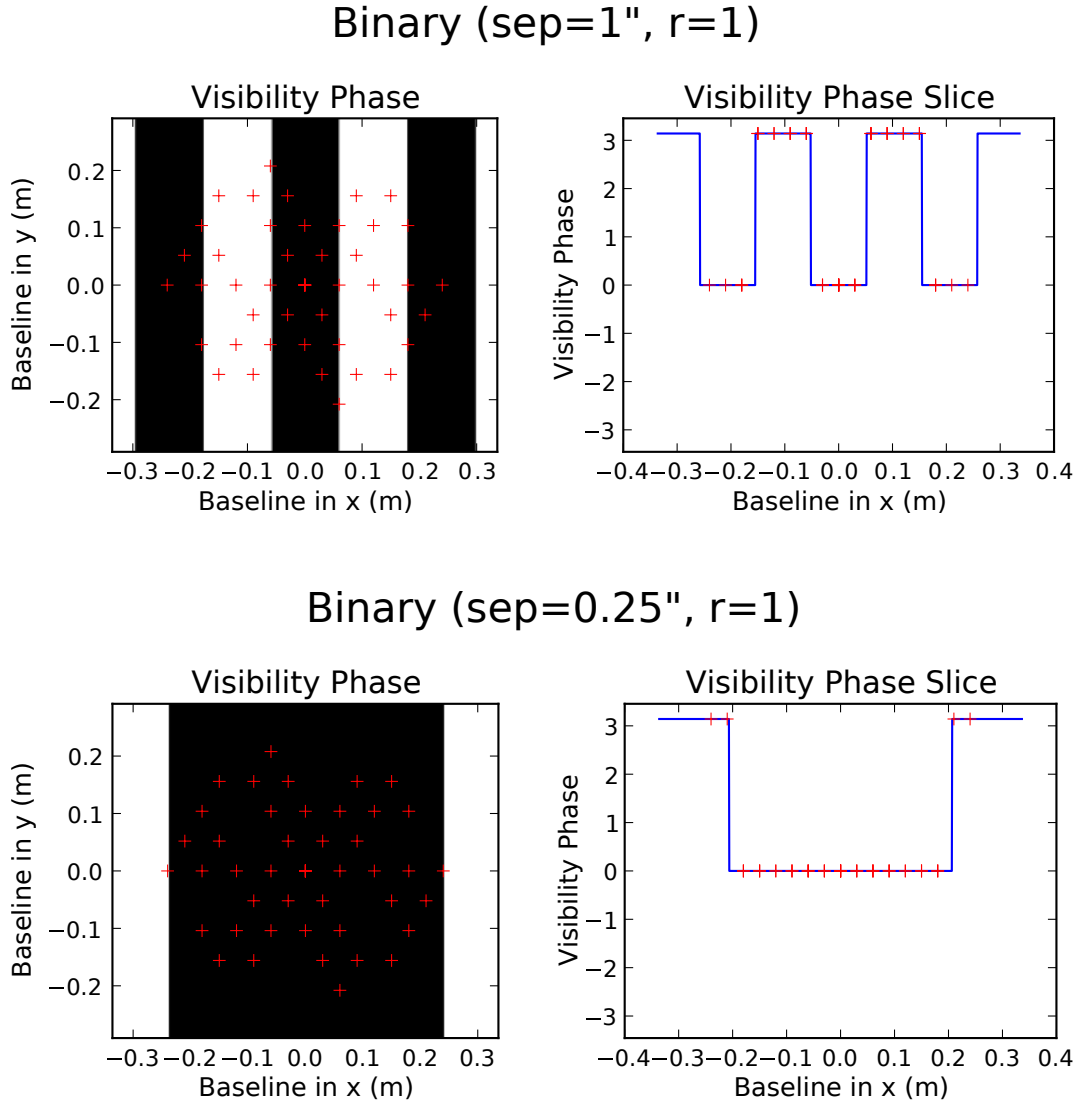


Fig. 2.— The visibilities for an equal binary at two different separations. The visibility phase is 0 or  $\pi$  radians and the stripes get stretched out when the separation becomes smaller. The crosses indicate the sampling points of our mask, see Section 3. The off-axis position was zero.

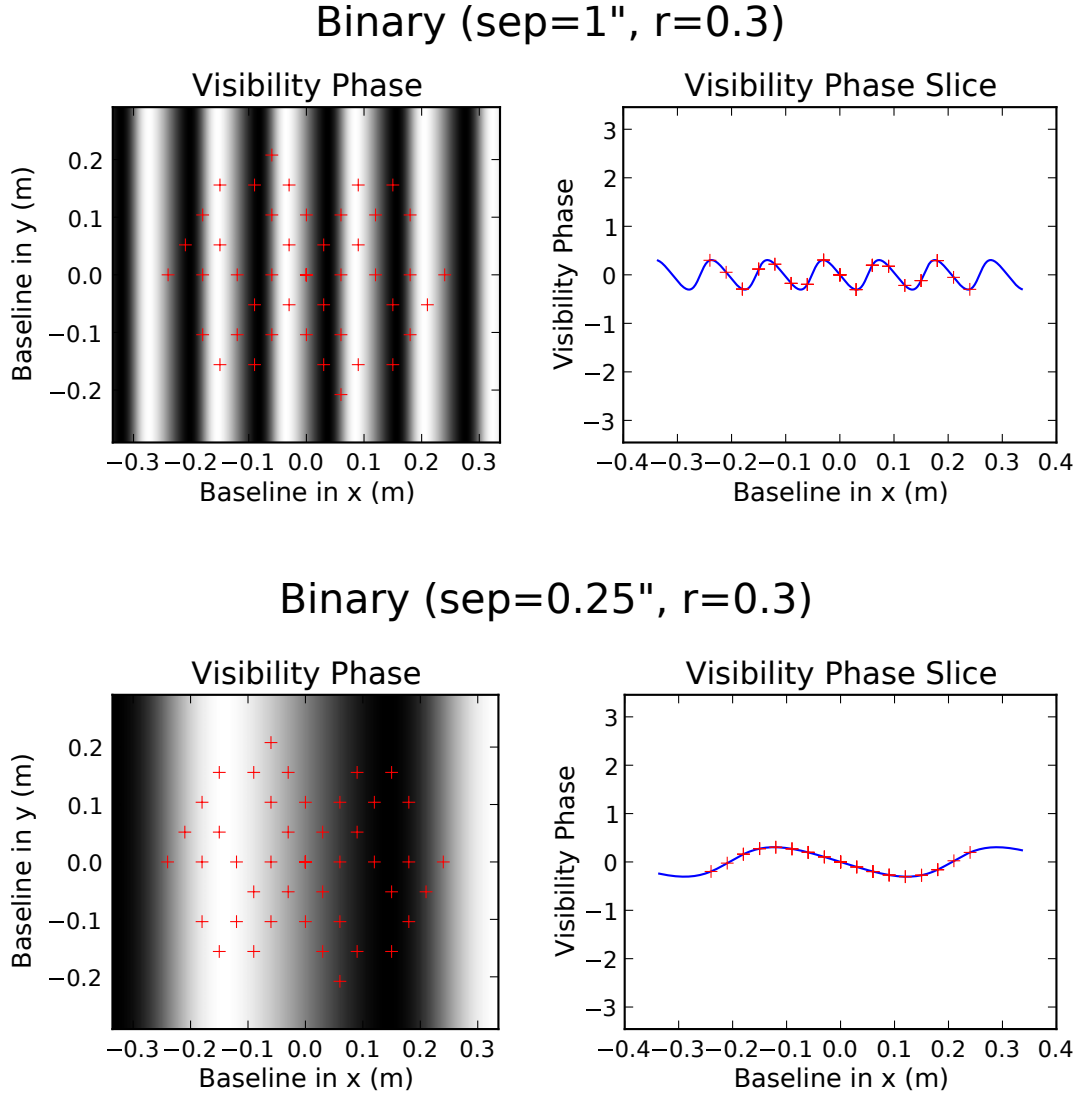


Fig. 3.— The visibilities for an equal binary at two different separations. The visibility phase is now a periodic function with an amplitude of  $\sim r$  radians. The phases have to be measured with greater accuracy if  $r$  is low, to be able to detect the binary. The off-axis position was set so that the primary star was located at the origin.

where  $\beta = (\beta_1, \beta_2, \dots, \beta_n)^\top$  is the vector of unknown coefficients of all fringes,  $\epsilon = (\epsilon_1, \epsilon_2, \dots, \epsilon_m)$  a vector of Gaussian distributed errors with mean 0 and variance  $\sigma^2$ , and  $X$  is the matrix of all linear sub-functions, given by:

$$X = \begin{pmatrix} X_{11} & X_{12} & \cdots & X_{1n} \\ X_{21} & X_{22} & \cdots & X_{2n} \\ \vdots & \vdots & \ddots & \vdots \\ X_{m1} & X_{m2} & \cdots & X_{mn} \end{pmatrix}. \quad (29)$$

If these sub-functions (the columns of  $X$ ) are linearly independent, which they are in a non-redundant mask, then the LLS-estimator or  $\beta$  is given by the *normal equations*:

$$(X^\top X)\hat{\beta} = X^\top \mathbf{y}. \quad (30)$$

or:

$$\hat{\beta} = (X^\top X)^{-1} X^\top \mathbf{y} \quad (31)$$

$$= X^+ \mathbf{y}, \quad (32)$$

where  $X^+$  is the *Moore-Penrose pseudoinverse* of  $X$ . This pseudo-inverse can be found easily (and numerically stable) using *singular value decomposition*. The variance-covariance matrix  $\Sigma_{\hat{\beta}}$  of this estimate is given by:

$$\Sigma_{\hat{\beta}} = \sigma^2 (X^\top X)^{-1}, \quad (33)$$

where  $\sigma^2$  can be estimated by unbiased estimator  $s^2 = \frac{S}{m-n}$ , and  $S = |X\beta - \mathbf{y}|^2$  is the sum of squares. The standard errors on  $\beta$  are the diagonal entries of this matrix. Plotting the residuals can uncover some more fitting errors, that aren't reflected in this standard error.

## 2.5. Averaging closure phases

Now that we have our theoretical closure phases, we have to fit these to our measured closure phases. Each measured closure phase for each frame is composed of three sources:

$$\tilde{\Phi}_{k,i} = \Phi_k + \beta_k + \xi_{k,i} \pmod{2\pi}, \quad (34)$$

where  $\tilde{\Phi}_{k,i}$  is the measured  $k$ -th closure phase in the  $i$ -th frame,  $\Phi_k$  is the intrinsic closure phase of the source,  $\beta_k$  is the systematic error on the  $k$ -th closure phase and  $\xi_{k,i}$  is the stochastic noise component of the  $k$ -th closure phase in the  $i$ -th frame. We will also define  $\phi_k = \Phi_k + \beta_k$ , for convenience later on.

First we have to average the closure phase over all frames. The modulo  $2\pi$  in the previous equation is no triviality: if we assume  $\xi_{k,i} \sim \mathcal{N}(\phi_k, \sigma_{k,i}^2)$ , then  $\tilde{\Phi}_{k,i}$  will have a so-called wrapped

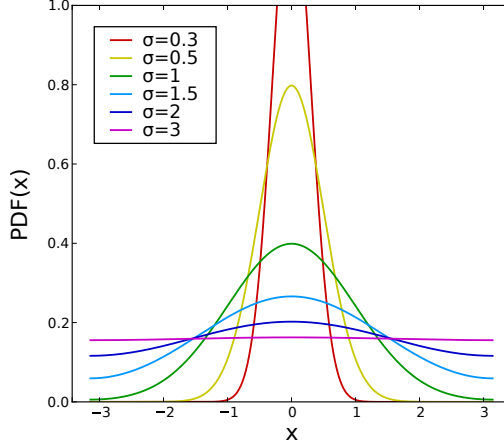


Fig. 4.— The Probability Distribution Function (PDF) for different values of  $\sigma$ . For this plot:  $\mu = 0$ . For small  $\sigma$ , the distribution is approximately a normal distribution. For large  $\sigma$ , it tends to an uniform distribution.

normal distribution. Note that the standard deviation  $\sigma_{k,i}$  of this normal distribution varies both with closure phase and frame. We can think of this as the standard error in  $\tilde{\Phi}_{k,i}$ .

In Figure 4 we can see this distribution for various values of  $\sigma_{k,i}^2$ . We can see that for values of  $\sigma_{k,i}$  larger than  $\sim 1$  radian the distribution becomes flatter and starts to look like a uniform distribution from  $-\pi$  to  $\pi$ .

There are different ways to fit circularly symmetric data, for example Coles (1998). These methods are optimal for small datasets and become more computationally complex as the dataset increases. As we have many ( $> 10000$ ) datapoints, these are computationally too expensive and we therefore use maximum likelihood estimators (MLE) in conjunction with wrapped distributions to fit the value of  $\phi_k$ . The Likelihood function  $\mathcal{L}$  is given by:

$$\mathcal{L}(\phi_k | \tilde{\Phi}_{k,1}, \sigma_{k,1}, \dots, \tilde{\Phi}_{k,N}, \sigma_{k,N}) = \prod_{i=1}^N f(\tilde{\Phi}_{k,i}, \sigma_{k,i} | \mu), \quad (35)$$

where  $f(x, \sigma | \mu)$  is the probability density function of the wrapped normal distribution with mean  $\mu$  and variance  $\sigma^2$  on position  $x$ , and  $N$  the number of frames. The maximalisation of this function  $\mathcal{L}(\phi_k)$  gives us the MLE  $\hat{\phi}_k = \arg \max \mathcal{L}(\phi_k)$ . We can estimate the error  $\hat{\sigma}_{\phi_k}$  on this estimate by using the Cramér-Rao lower bound and the Fisher information as follows:

$$\hat{\sigma}_{\phi_k} = \frac{1}{I(\hat{\phi}_k)}, \quad (36)$$

where  $I(\phi_k)$  is the Fisher information defined by:

$$I(\phi_k) = -\mathbb{E} \left[ \frac{\partial^2 \log \mathcal{L}(\phi_k)}{\partial \phi_k^2} \right] \quad (37)$$

The need for calibrating for the systematic errors  $\beta_k$  is still left. We can estimate these systematic errors by observing a single star. This single star has a closure phase of zero everywhere, so such a measurement directly results in  $\hat{\beta}_k$ . Then, we can subtract this from our observed closure phases for the binary to get  $\hat{\Phi}_k$ :

$$\hat{\Phi}_k = \hat{\phi}_k - \hat{\beta}_k \quad (38)$$

Note that this calibration doesn't get rid of all systematic errors. For instance, bandwidth errors due to a different spectrum of the single star compared to the binary still exist.

## 2.6. Binary parameter estimation

When we have the measured closure phases of our binary, we need to fit a binary to these closure phases. The easiest way is to do a Non-Linear Least Squares (NLLS) fit. We also need to take care with the wrapping nature of phase when doing so. The sum of squares is given by:

$$SS_{\text{binary}}(\{\hat{\phi}_k\} | \vec{\rho}/\lambda, r) = \sum_{k=1}^K \min_{\ell=-\infty}^{\infty} \frac{(\hat{\phi}_k - \arg(B_{\text{binary}}(\vec{b}_{k,1}, \vec{b}_{k,2} | \vec{\rho}, \lambda, r)) + 2\pi\ell)^2}{\sigma_{\hat{\phi}_k}^2}, \quad (39)$$

where  $K$  is the total number of closure phases,  $\sigma_{\hat{\phi}_k}$  the standard error on the estimate of  $\phi_k$ , and  $\vec{b}_{k,1}$  and  $\vec{b}_{k,2}$  the first and second baseline of the  $k$ -th closure phase. Note that  $\vec{\rho}/\lambda$  is the parameter, instead of the separation and wavelength separately. Doing the latter, we would create an ambiguity in the optimisation procedure. This ambiguity is easily visible in the equations for  $B_{\text{binary}}(\vec{b}_1, \vec{b}_2)$ , as those are dependent on  $\vec{\rho}/\lambda$  and not on the variables separately.

That we can generate a correct fit is not that impressive. We need to find the statistical significance of the statement that we have found a binary. This can be done by hypothesis testing, as worked out by Bernat (2012). He used an F-like-test to discard the null-hypothesis that states that the star is single. We'll use the conventional F-test instead. The F-value is calculated by dividing two Chi-squared distributed variables, namely the sum of squares if the star is a binary, and the sum of squares if the star is single. The latter is given by:

$$SS_{\text{single}}(\{\hat{\phi}_k\}) = \sum_{k=1}^K \min_{\ell=-\infty}^{\infty} \frac{(\hat{\phi}_k + 2\pi\ell)^2}{\sigma_{\hat{\phi}_k}^2}. \quad (40)$$

This gives the F-value:

$$F = \frac{SS_{\text{single}}(\{\hat{\phi}_k\})}{\min_{\vec{\rho}/\lambda, r} SS_{\text{binary}}(\{\hat{\phi}_k\} | \vec{\rho}/\lambda, r)} - 1. \quad (41)$$

The null-hypothesis is discarded if the F-value is smaller than the critical F-value  $F_{\text{crit}}$ , so that larger values of  $F$  signify a better fit. If the errors are normally distributed and independent, the F-value is distributed as an F-distribution, under the null-hypothesis. For now we will assume this is the case, so that the p-value of the binary detection can be easily calculated.

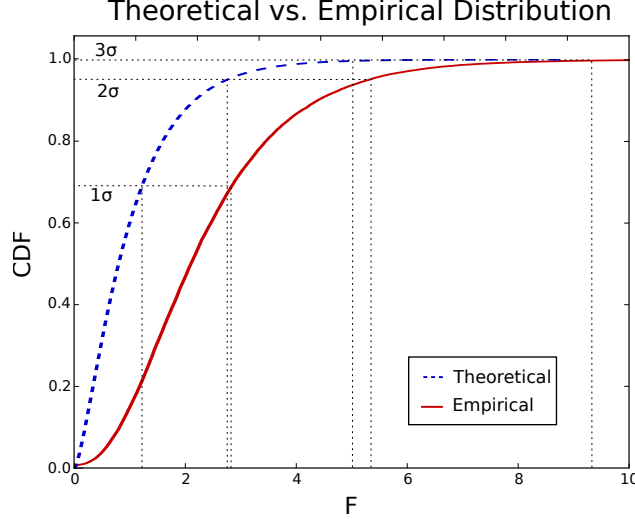


Fig. 5.— The theoretical and empirical cumulative distribution function (CDF) of  $F$  under the null-hypothesis. We can see that the  $1\sigma$ ,  $2\sigma$  and  $3\sigma$  critical  $F$ -values are significantly lower for the theoretical value. The empirical distribution retains closure phase correlations, and is therefore the distribution to use. The final critical  $F$ -values were  $\sim 2.80$ ,  $\sim 5.40$  and  $\sim 9.22$  for the  $1\sigma$ ,  $2\sigma$ , and  $3\sigma$  confidence levels respectively.

If this is *not* the case, this critical  $F$ -value can be found using Monte-Carlo simulations of the noise of the closure phase data. For each of the many simulated observations, we generate a random sample with replacement from our frames data, similar to the statistical method *bootstrap*. We calculate the closure phases in the usual way, and do the same for the calibrator measurements. We then record the  $F$ -value for each of these simulated observations. This gives us the distribution of the  $F$ -value under the null-hypothesis, and therefore the p-value of our real detection. As bootstrap doesn't assume that the errors are normally distributed, it preserves all correlations between the closure phases, and is therefore less biased. [Bernat \(2012\)](#) showed that finding  $F_{\text{crit}}$  with Monte-Carlo is more conservative than analytical hypothesis testing. This is also visible in our data, as shown in Figure 5.

Another useful plot is the contrast limit plot. This plot indicates, if we didn't see a binary, what sort of binary we could have seen, if it was there, given the error characteristics of the data. This plot gives for each position of the secondary star the maximum contrast at which the binary would be detected at  $n\sigma$  confidence. In formula form, we are displaying the function  $f(\rho)$ :

$$f(\rho) = \arg \min_r \left| \Pr(F > F_{\text{crit}}) - \text{erf} \left( \frac{n}{\sqrt{2}} \right) \right|, \quad (42)$$

where  $\text{erf}(x)$  is the (Gauss) error function. We can calculate  $f(\rho)$  by simulating an observation of a binary at the specified  $\rho$  and a contrast of  $r = 1$ , using the noise characteristics of the data. We can then fit the binary and retrieve the probability of actually detecting the binary by repeating

this for many simulated realisations of the noise. We can then lower the contrast of the simulated binary until we detect the binary at  $n\sigma$  confidence. We have to repeat this for every  $\rho$  to get a contrast limit plot. We can see such a plot on our data in Figure 33.

### 3. Mask Design

#### 3.1. Introduction

In this section, we discuss the design of the mask. The requirements and criteria of a non-redundant mask are established in Subsection 3.2. In Subsection 3.3 we describe the algorithms used to create a mask that complies with the requirements and criteria discussed before. Our own mask is shown as a result of these algorithms in Subsection 3.4 and possible improvements are described in Subsection 3.5.

#### 3.2. Requirements and criteria

The designed mask has to satisfy some requirements to be able to use it for Sparse Aperture Masking. On top of that, we need to maximize some criteria to get an optimal mask. In this section, we list the requirements and criteria that we use to determine our masks.

##### 3.2.1. Requirements

To be able to trace a fringe back to only one pair of holes, we need to have a *non-redundant* mask. Because each fringe (its direction and frequency) is uniquely determined by a baseline (its direction and length), this means that a certain baseline has to exist only once on the mask to be able to trace the fringe back to a pair of sub-apertures. This may seem more simple than it looks: within one subaperture, there is always some redundancy. This redundancy can be ignored however, if the holes are smaller than the Fried parameter, as was shown by Noll (1976) and Roddier (1981). This subaperture redundancy also means that the baselines have a finite width in the uv-plane.

Another requirement is that the holes have to be fully illuminated to be able to use them for interferometry. Partial obstruction leads to anomalously low power for the baselines involving that hole (Tuthill 1994). Obstruction must therefore be avoided. The most important obstructions to worry about are the central obscuration, due to the secondary mirror, and the support structure of the secondary mirror.

### 3.2.2. Criteria

To get the most information out of an observation with the mask, it has to have as many baselines as possible. The more holes the mask has, the more baselines it has and the better it is at observing a binary. We could easily achieve this by making the holes very small, but then we would have very little signal going through our mask, which makes it harder to detect a binary. Optimal performance of a mask is reached if the subapertures have a diameter of the Fried parameter (Bernat 2012; Fried 1965).

Because the mask has to be non-redundant there is some choice as to where to put the baselines. To be able to detect binaries in various orientations on the sky and various separations, we need to have the baselines distributed as uniform as possible in the uv-plane. This is also known as *uniform uv-coverage*.

In our case, we decided to maximize uv-coverage without compromising non-redundancy by observing with two orientations of the mask. Because our telescope has four radially symmetric spiders, the obvious choice is to turn the mask 90 degrees. In this way, we ensure secondary mirror support structure avoidance in both orientations at the same time.

## 3.3. Algorithms

For small masks (masks with large holes) the optimal mask can be found by listing each mask and choosing the best one. This algorithm is also known as *brute-force*. For larger masks this isn't viable anymore. In those cases, we have chosen to use *iterative* algorithms. These algorithms place a hole at the optimum position as determined on the incomplete mask. Although it is not guaranteed to give us the best mask, it gives a good, if not the best, mask in most cases. We'll also see that the brute-force algorithm can be easily implemented as an iterative algorithm.

Some of our mask-design algorithms are based on those described in a paper by Carlotti and Groff (2010). Some details in this paper were vague or left out completely. We therefore try to explain these clearer and in a more mathematical and algorithmic fashion. In these subsections we discuss how to (quickly) determine beforehand if a mask is going to be redundant and how to determine the best position of the next subaperture. We also describe how we chose the final mask.

### 3.3.1. Triple correlation

We use the Triple Correlation (TC) to determine if the location of the next subaperture makes the mask redundant. To see what the triple correlation of a mask is, we write the mask as a

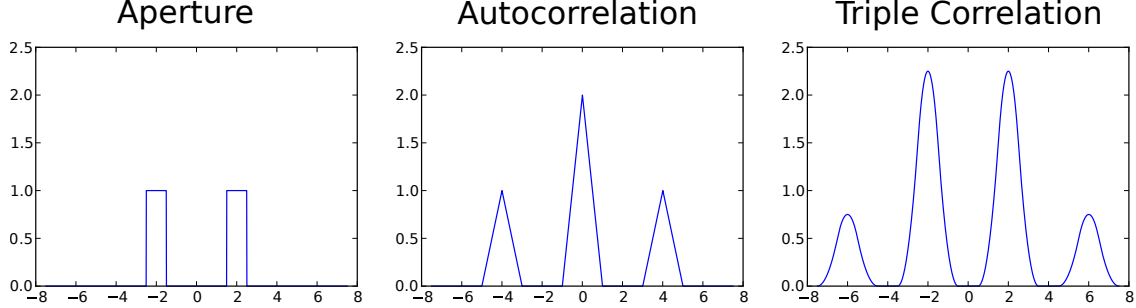


Fig. 6.— The autocorrelation (middle) and triple correlation (right) for a 1D mask (left). We can see the three peaks as baseline coverage in the autocorrelation. We can also identify three possible positions for the next sub-aperture:  $x = \pm 4$  and  $x = 0$ .

convolution of a single sub-aperture with a sum of delta functions:

$$M_N(\mathbf{x}) = \sum_{i=1}^N \Pi(\mathbf{x} - \mathbf{p}_i) \quad (43)$$

$$= \left( \sum_{i=1}^N \delta(\mathbf{x} - \mathbf{p}_i) \right) \otimes \Pi(\mathbf{x}), \quad (44)$$

where  $\otimes$  denotes convolution,  $M_N(\mathbf{x})$  is the mask with  $N$  subapertures,  $\delta(\mathbf{x})$  is the Dirac delta function,  $\mathbf{p}_i$  the position of the  $i$ -th subaperture and  $\Pi(\mathbf{x})$  is the aperture function of a single subaperture, defined by:

$$\Pi(\mathbf{x}) = \begin{cases} 1 & \text{if } |\mathbf{x}| < \frac{d}{2} \\ 0 & \text{otherwise} \end{cases}. \quad (45)$$

Using basic rules for convolution and cross correlation we can prove that:

$$M_N \star M_N = \left( \sum_{i,j}^N \delta(\mathbf{x} - \mathbf{b}_{ij}) \right) \otimes (\Pi \star \Pi), \quad (46)$$

where  $\star$  denotes cross correlation and  $\mathbf{b}_{ij} = \mathbf{p}_i - \mathbf{p}_j$  is the baseline between the subapertures  $i$  and  $j$ . In the same way, we can write the triple correlation:

$$M_N \star M_N \star M_N = \left( \sum_{i,j,k}^N \delta(\mathbf{x} - (\mathbf{p}_k - \mathbf{b}_{ij})) \right) \otimes (\Pi \star \Pi \star \Pi) \quad (47)$$

We can see that where the triple correlation is non-zero, you can't place an aperture, because then you are duplicating an existing baseline. There is only one case where the resulting mask is still redundant, even if the triple correlation is zero. This case arises when the two redundant baselines did not exist before: they were both created when placing the subaperture. This can be handled separately, as the only position where this is possible, is in the middle of two existing subapertures.

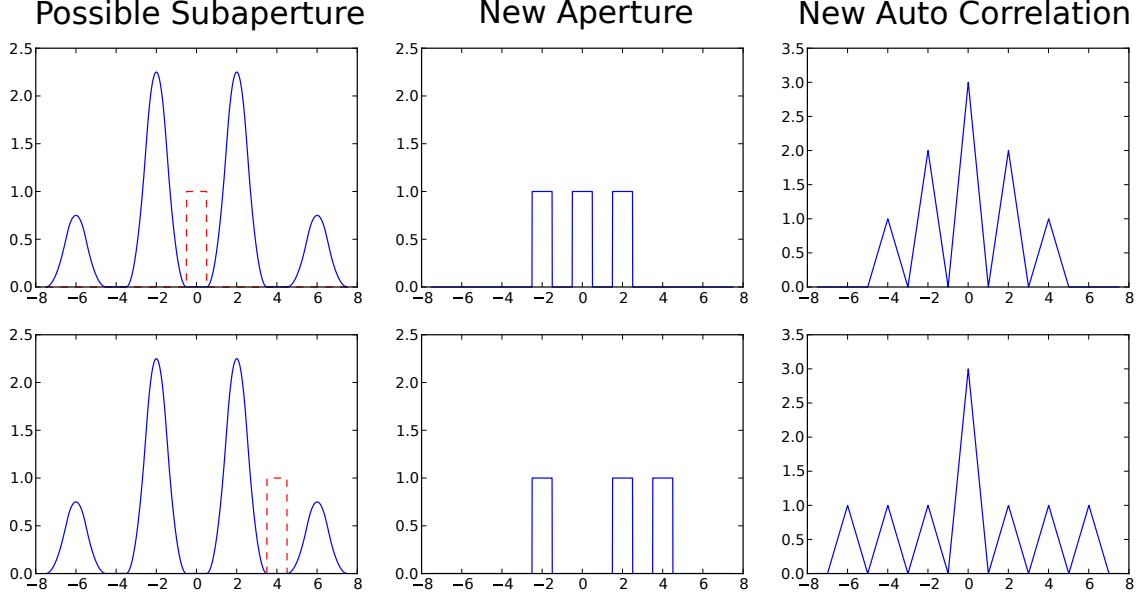


Fig. 7.— The possible positions for a next subaperture for the mask of Figure 6. The new sub-aperture at  $x = 0$  leads to a redundant mask (upper row), while the one at  $x = \pm 4$  does lead to a non-redundant mask (lower row). This can be seen in the height of the peaks in the autocorrelation (right column).

We can see an example in only one dimension in Figures 6 and 7. The auto-correlation identifies, along with countless other further away from the center, three positions for the next sub-aperture:  $x = \pm 4$  and  $x = 0$ . These are both worked out in Figure 7. The position  $x = 0$  leads to a redundant mask, because it is in the center of two existing baselines, and therefore creates two identical baselines. The other position leads to a non-redundant mask as expected.

### 3.3.2. Criteria

Now that we know when the position of the next subaperture makes the resulting mask redundant, we have to choose between these possible points. This is done by calculating certain criteria. Carlotti and Groff describe three possible criteria. We only describe the last of these, namely “Algorithm Two”. This algorithm maximizes the distance with respect to the existing subapertures. The criterion is therefore:

$$C(\mathbf{x}) = \sum_{i=1}^N |\mathbf{x} - \mathbf{p}_i|, \quad (48)$$

where  $C(\mathbf{x})$  is the criterion evaluated at position  $\mathbf{x}$ . If the criterion for one possible position and another is the same, we’ll try both recursively. This procedure generates a tree of possible masks. The leaves of this tree are the final masks and each branch adds another subaperture to the (partial)

mask.

We are still left with an infinite number of possible next subapertures to check. This problem can be solved by checking only subaperture positions that lie on a grid. The baselines then also lie on the same grid. Because we want the baselines in the uv-plane to lie as close together as possible, we use a hexagonal grid, as it's the closest packing of circles on a 2D space. Additionally, the possible sub-apertures must not be located on the central obscuration. The obstruction by the spiders is handled later on.

We can see that the brute force method can be easily implemented using a flat criterion: this criterion doesn't display any preference between the possible subapertures, so that all possible sub-apertures have to be checked, and therefore all non-redundant masks are listed recursively.

### 3.3.3. Mask choice

After these algorithms, we are left with a list of masks, which can be very long, especially in the case of a flat criterion (brute-force). We therefore have to filter some cases out automatically, before choosing the best mask manually:

- Masks with fewer subapertures than the maximum possible are discarded immediately for reasons described before.
- Rotated and/or mirrored masks are also discarded, as they don't contribute to qualitatively different masks.
- Masks that overlap the secondary mirror support structure under every orientation.

Now that this list has shrunk dramatically, we have to choose the best mask by hand. The only criteria left is the uniform uv-coverage, which can be analysed by three plots: the baseline coverage (the autocorrelation of the mask) and its projections, the radial and azimuthal baseline density plots. We'll choose the mask with the most uniform sampling coverage in the uv-plane, and the most constant line in the radial and azimuthal density plots. An example of such plots for simple two and three hole masks are shown in Figure 8.

## 3.4. Results

We have chosen our final mask with  $D/r_0 = 10$ , using a brute force optimisation using the triple correlation and with all holes on a hexagonal grid. This produced seven masks, which are displayed in Figure 9. Two of these masks also resulted from using the Algorithm Two criterion. The characteristics of the chosen mask are shown in Figure 10.

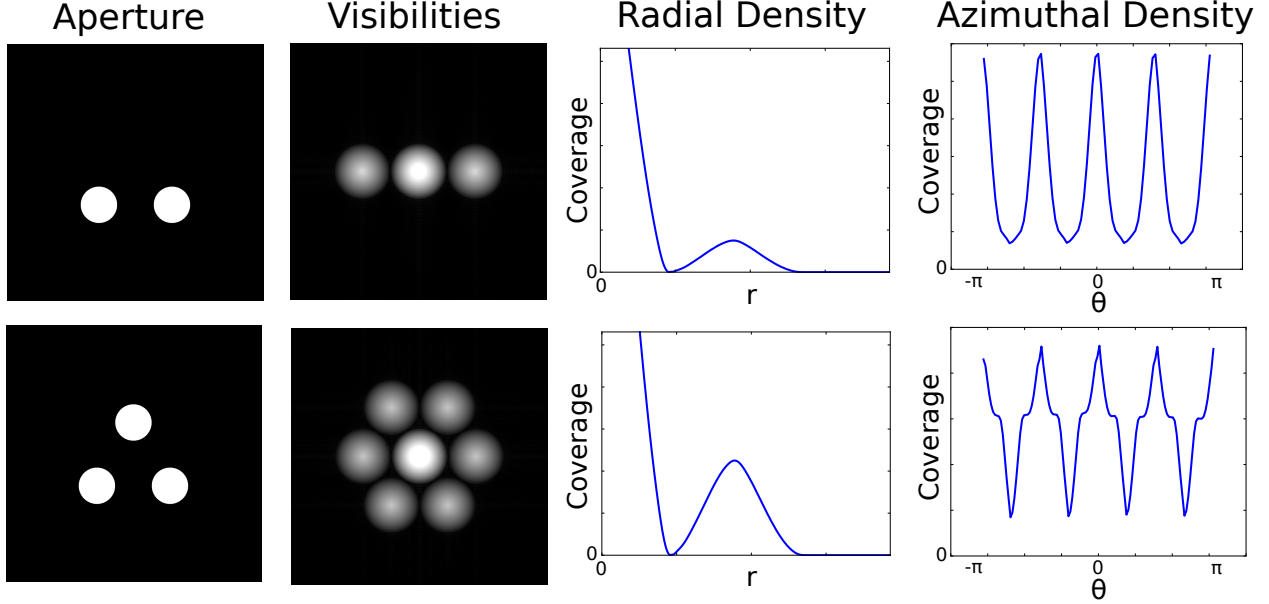


Fig. 8.— The different kind of plots that are useful when choosing the correct mask: the aperture of the mask (first column), the visibility plane (second column), the radial (third column) and azimuthal (fourth column) baseline density plots. These density plots also include the turning of the mask by  $90^\circ$ , as is not shown in the visibilities. In choosing the final mask, the sampling of the visibility plane, including turned version, has to be as uniform as possible, and the densities as constant as possible.

### 3.5. Possible improvements

Although all the created masks were non-redundant and applicable for our use, there are a lot of things not taken into account when creating our masks:

- *Closure triangle shapes.* For probing different aspects of a source, we can employ different kinds of closure phases. For our binary, we need to use closure triangles with all long baselines. This increases the closure phase for high-contrast binaries. In Monnier (2007) we can see this idea implemented for a star with dust shell model.
- *Bandwidth corrections.* All the PSF's shown before were made with monochromatic light. In reality, we need to use a finite bandwidth, which can be as large as 20% of our central wavelength. This has the effect of radially blurring the visibility plane. In Figure 11 we can see this effect. Our splodges now start to overlap, and therefore the fringe visibility lowers. We can compensate for this by changing the positions of the holes slightly, giving the visibility splodges more room to expand radially. This means that sub-optimal masks may become optimal when the bandwidth is taken into account, which makes this optimisation more computationally expensive.

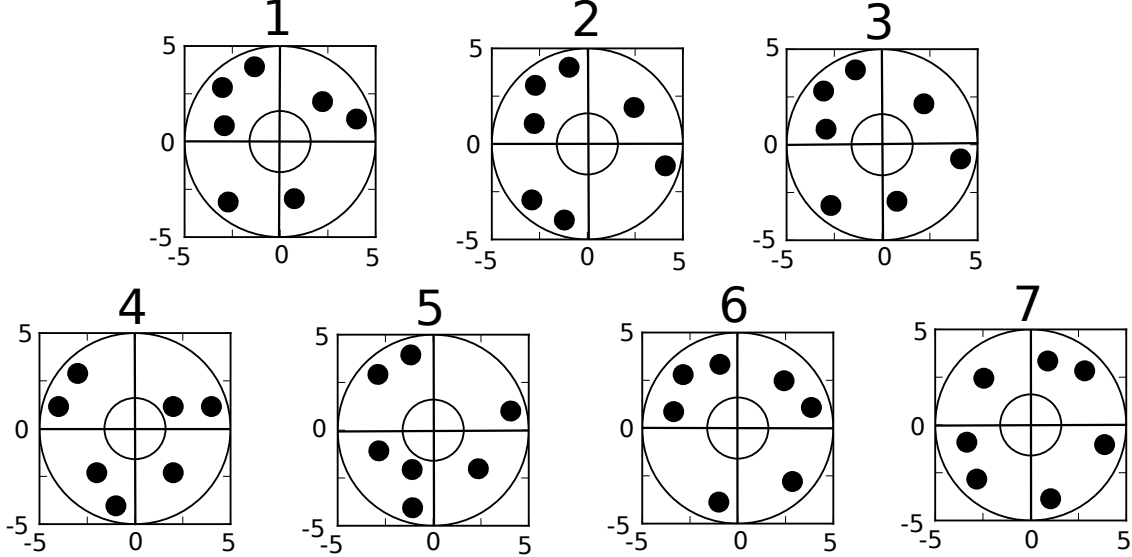


Fig. 9.— The five resulting masks at  $D/r_0 = 10$ . The units on the axes are in  $r_0$ . The outer edge, the central obscuration and the spiders of the telescope are also plotted. The chosen mask was mask nr. 4. Note that mask nr. 6 is identical to the layout chosen by Sivaramakrishnan et al. (2010) for the JWST. This mask is sub-optimal when we take the turning of the mask into account.

- *Non-grid solutions.* We have also restricted the search for new sub-apertures to positions on a grid. We can relax this assumption by subdividing this grid by a factor  $f$ . The algorithm didn't seem to choose these positions more often, and the resulting masks were often small translational variations of the mask, which doesn't matter for the final result. Additionally, the complexity of these subdivisions is  $O(f^2)$ , which makes high factors computationally unfavorable. Other optimisation methods, instead of brute force searching for the optimal next sub-aperture, have not been implemented.
- *Non-iterative optimization.* We also assume that choosing the optimal next sub-aperture for each mask leads to the best mask in the end. This is not always the case and this leads optimisation of all sub-apertures at once. The complexity introduced is  $O(n_{\text{holes}})$ , where  $n_{\text{holes}}$  is the number of sub-apertures.

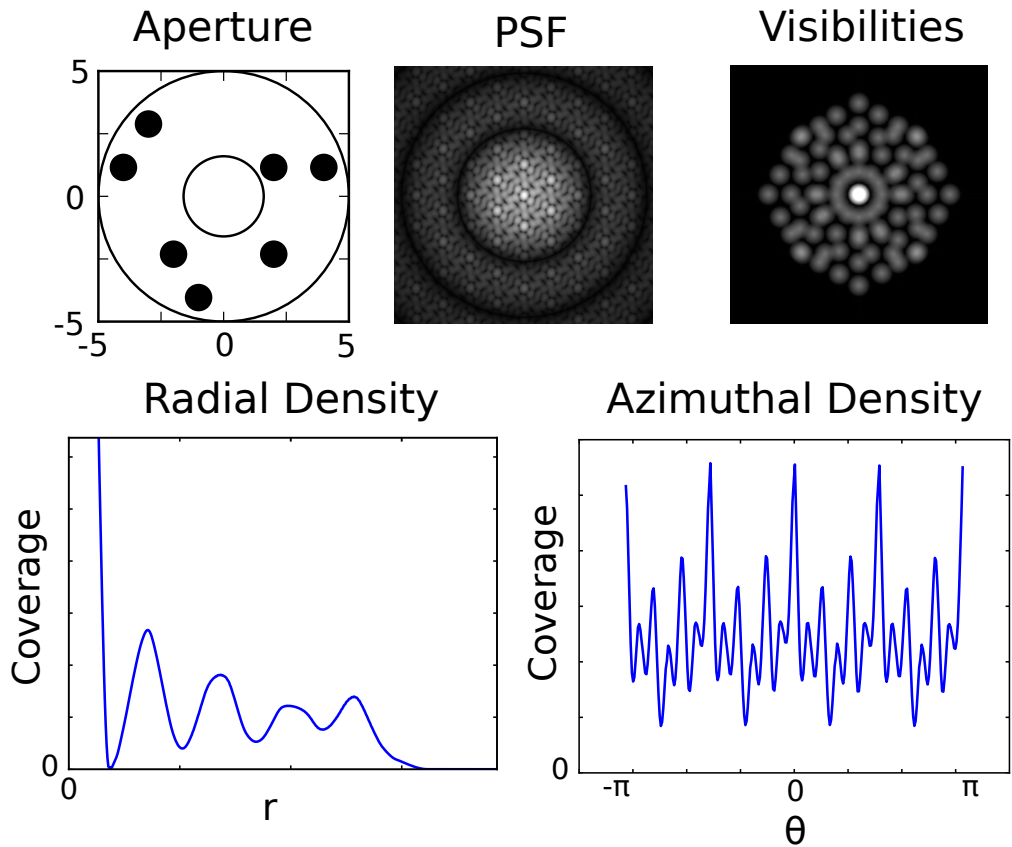


Fig. 10.— The characteristics of our mask. The mask itself (upper left), its PSF (upper middle) and the visibility plane including turned mask contribution (upper right). The coverages of radial (lower left) and azimuthal density (lower right) are also shown. The visibility plane is very uniformly sampled, which should result in many visible binaries.

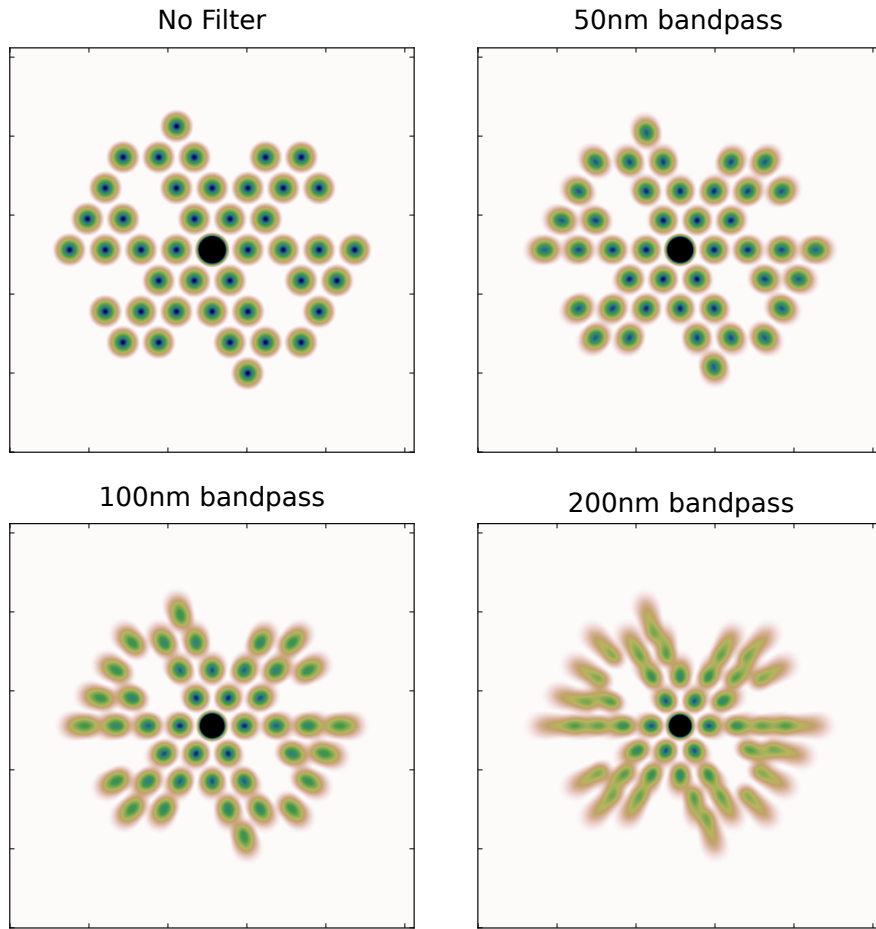


Fig. 11.— The effects on a non-zero bandwidth in the uv-plane. As the bandwidth becomes larger, the splodges start to overlap as the whole uv-plane radially blurs. This introduces phase errors as well as decoherence. The central splodge is thresholded to show more detail in the non-redundant part. The colourscale has been inverted.

## 4. Modeling and simulating seeing

### 4.1. Introduction

We can view the light coming from a star to be a perfectly flat plane wave. This perfect wavefront is distorted by the atmosphere as the starlight travels through turbulent cells, which have different indices of refraction. After propagation through the atmosphere, the wavefront has been changed in both phase and amplitude. The phase distortion however, is much more detrimental to our image compared to the amplitude distortion, and therefore the latter is often ignored.

These phase distortions can be described using models. The most important are the Kolmogorov model (Kolmogorov 1941) and the Von Kármán model (Diederich and Drischler 1957). For a nice explanation of the differences between these two models, see Floyd et al. (2010). We use the Kolmogorov model for simplicity, and give a short summary of the statistics of Kolmogorov phase screens in Subsection 4.2. We describe the conventional approach to creating phase screens in Subsection 4.3 and our new method in Subsection 4.4. The method for time-dependent phase screens is shown in Subsection 4.5. The phase screens are normalised in Subsection 4.6.

### 4.2. Kolmogorov theory

The phase screen  $\phi(\mathbf{r})$  is a function of position on the aperture  $\mathbf{r} = (x, y)$ . We can write this phase screen in terms of its Fourier transform  $\Phi(\mathbf{k})$ :

$$\phi(\mathbf{r}) = \int_{-\infty}^{\infty} \int_{-\infty}^{\infty} \Phi(\mathbf{k}) \exp(2\pi i \mathbf{k} \cdot \mathbf{r}) d\mathbf{k}, \quad (49)$$

$$\Phi(\mathbf{k}) = \int_{-\infty}^{\infty} \int_{-\infty}^{\infty} \phi(\mathbf{r}) \exp(-2\pi i \mathbf{k} \cdot \mathbf{r}) d\mathbf{r}. \quad (50)$$

An easily observable property of the phase screen is the phase structure function  $D(|\mathbf{r}|)$ . This function describes the variance of the phase at two different points of the aperture of the telescope. We'll call these points  $\mathbf{r}_1$  and  $\mathbf{r}_2$ . The phase structure function is then given by:

$$D(|\mathbf{r}_2 - \mathbf{r}_1|) = \langle (\phi(\mathbf{r}_1) - \phi(\mathbf{r}_2))^2 \rangle \quad (51)$$

where  $\langle \cdot \rangle$  denotes the expectation value over the ensemble. The phase structure function depends on the turbulence of the atmosphere. For Kolmogorov turbulence, the phase structure function is defined by:

$$D(|\mathbf{r}|) = 6.88 \left( \frac{|\mathbf{r}|}{r_0} \right)^{\frac{5}{3}}, \quad (52)$$

where  $r_0$  is the Fried parameter (Fried 1965). Using this phase structure function we can derive the power spectrum of our phase screen, as Noll (1976) showed:

$$D(|\mathbf{r}|) = 2 \int \Psi(\mathbf{k}) [1 - \cos(2\pi \mathbf{k} \cdot \mathbf{r})] d\mathbf{k}, \quad (53)$$

where  $\Psi(\mathbf{k}) = |\Phi(\mathbf{k})|^2$  is the Wiener spectrum of the turbulence. For Kolmogorov turbulence, he found that:

$$\Psi(\mathbf{k}) = 0.023r_0^{-\frac{5}{3}}|\mathbf{k}|^{-\frac{11}{3}}. \quad (54)$$

Therefore:

$$|\Phi(\mathbf{k})| \propto r_0^{-\frac{5}{6}}|\mathbf{k}|^{-\frac{11}{6}} \quad (55)$$

$$\phi(\mathbf{r}) \propto r_0^{-\frac{5}{6}}. \quad (56)$$

We can see that for  $|\mathbf{k}| \rightarrow 0$  the power spectrum becomes infinite. Most of the power of the Kolmogorov turbulence is therefore captured in low frequencies. We can also see that we can scale the phase screen to any Fried parameter, after we have created it, using Equation 56.

Another important property of Kolmogorov turbulence is its fractal nature. That means that, under the right phase scaling conditions, the phase screen looks similar at whatever spatial scale you are looking. This property is a direct consequence of the power law nature of the power spectrum of Kolmogorov turbulence. In the phase structure function, this phase scaling condition looks as follows for  $\alpha$  the spatial scaling factor:

$$D(\alpha|\mathbf{r}|) = \alpha^{\frac{5}{3}}D(|\mathbf{r}|). \quad (57)$$

In reality, the true atmospheric turbulence does not have an infinite extent in the power spectrum. It only approximates theoretical Kolmogorov turbulence over the *inertial range*:

$$\ell_0 < |\mathbf{r}| < L_0, \quad (58)$$

where  $\ell_0$  and  $L_0$  are the inner and outer scale respectively. Typical values are a few millimeters for the inner scale and between 2 to 100 meters for the outer scale, see Lane et al. (1992). A diagram containing Kolmogorov power spectrum including inertial range is shown in Figure 12.

### 4.3. Conventional approach

Using this theory, we rewrite this problem in a sampled representation. The matrix of  $\Phi(\mathbf{k})$  becomes the matrix  $Q$ :

$$Q_{k\ell} = \sqrt{0.023}(k^2 + \ell^2)^{-\frac{11}{12}} \exp(i\theta_{k\ell}), \quad (59)$$

where  $Q_{k\ell}$  is the index  $(k, \ell)$  of the matrix  $Q$  and  $\theta_{k\ell} \sim U(0, 2\pi)$  is a random variable dependent on indices  $k$  and  $\ell$ , which represents the random uniformly distributed phase of the spectrum. The Fried parameter is set to one pixel for convenience, as we can scale the phase screen to the correct Fried parameter later on, given Equation 56.

Then the phase screen  $R_{mn}$  is given by the inverse discrete Fourier transform:

$$R_{mn} = \frac{1}{MN} \sum_{k=-\frac{M}{2}}^{\frac{M}{2}-1} \sum_{\ell=-\frac{N}{2}}^{\frac{N}{2}-1} Q_{k\ell} \exp\left(2\pi i \left[\frac{km}{M} + \frac{\ell n}{N}\right]\right), \quad (60)$$

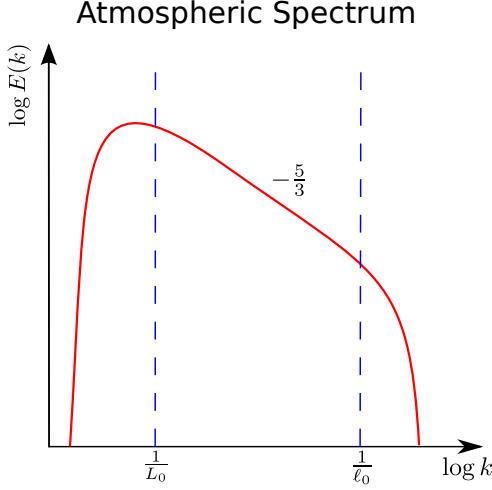


Fig. 12.— A diagram containing a Kolmogorov power spectrum over an inertial range. Within this inertial range the spectrum is a  $-\frac{5}{3}$ -power law. Our model doesn't use this inertial range.

where  $M$  and  $N$  are the length of the arrays created. Note that when the  $Q_{k\ell}$  is point symmetric around the zero frequency, then the discrete Fourier transform, instead of its inverse, also gives a correct phase screen. The real part of this matrix (and also its imaginary part) is a phase screen with the correct power law, but still unnormalised.

A side effect of a sampled representation is that the phase screen is periodic, which is unlike the theoretical phase screens. Therefore, the phase structure function is also periodic and departs from the theoretical phase structure function when we reach that periodicity. This can be seen in Figure 13).

To capture all the frequencies in the inertial range of the turbulence, we need a lot of samples. Let us choose  $\ell_0 = 1$  mm and  $L_0 = 50$  m, which are both reasonable values. Then we need at least  $M, N = L_0/\ell_0 = 50000$  linearly spaced samples. A discrete Fourier transform of this size takes a very long time. Therefore we need to make approximations to make this Fourier approach feasible.

One of those approximations is to only calculate the phase screen on top of the aperture, instead of a square of  $L_0$  by  $L_0$ . Because of the periodicity of the phase screen, this doesn't give good results. Some, for example [McGlamery \(1976\)](#), have tried calculating the phase screen over a larger area, for example  $4D$  by  $4D$ , where  $D$  is the diameter of the aperture, and only use the middle part of this phase screen. As [Lane et al. \(1992\)](#) showed, this yields a significant improvement, but comes at 16 times the cost of a single phase screen.

Another approach was to approximate the low frequencies that were discarded by a tip-tilt of the phase screen, according to centroid shift statistics, see [Roddier \(1981\)](#) and [Shaklan \(1989\)](#). As [Lane et al. \(1992\)](#) noted, this doesn't account for all the information that low frequencies provide.

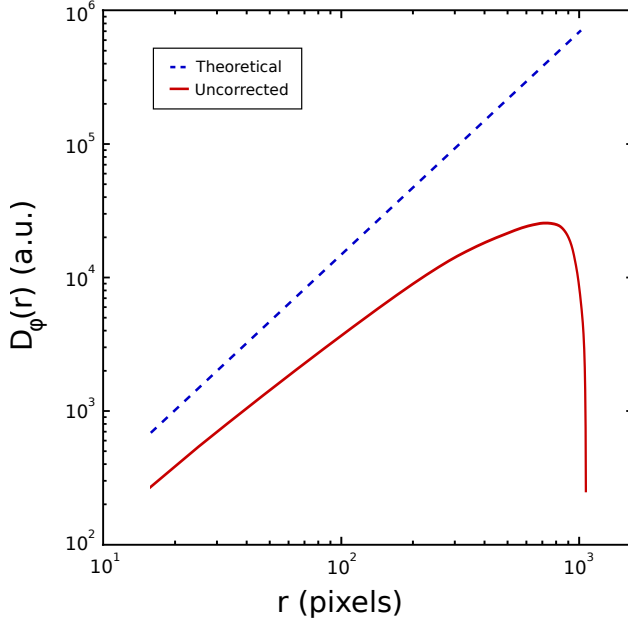


Fig. 13.— The phase structure function of an uncorrected phase screen departs from the theoretical phase structure function to reach zero at the end of the phase screen. We want to avoid this behaviour by including subharmonics.

Lane et al. (1992) therefore proposed manually adding those low frequencies using the spectral leakage of subharmonic components. The zero frequency component is subdivided into nine equally spaced samples, which they call a subharmonic set. This is done recursively to reach the required number of subharmonic sets. The generated samples are shown in Figure 14. Because this resulting set of samples is not equally spaced anymore, we can't use a Fast Fourier Transform (FFT) to Fourier transform this data, which is a serious disadvantage in computational efficiency.

#### 4.4. Our method

Our method of adding subharmonics to the phase screen is based on scale separation. We'll compose our final phase screen out of two phase screens, in the same way as Xiang (2012):

$$\phi(\mathbf{r}) = \phi_{\text{FFT}}(\mathbf{r}) + \phi_{\text{low}}(\mathbf{r}), \quad (61)$$

where  $\phi(\mathbf{r})$  is our final phase screen,  $\phi_{\text{FFT}}(\mathbf{r})$  is the phase screen generated by conventional methods, and  $\phi_{\text{low}}(\mathbf{r})$  is the phase screen that corrects for subharmonics that aren't captured in  $\phi_{\text{FFT}}(\mathbf{r})$ . In our approach, the correcting phase screen is an part of an oversampled version of another phase screen  $\phi_{\text{low,harm}}(\mathbf{r}) = \phi_{\text{low}}(\beta\mathbf{r})$  that contains all subharmonics as harmonics, where  $\beta > 1$  is the factor of oversampling. This means that we can  $\phi_{\text{low,harm}}(\mathbf{r})$  using normal FFT techniques. The

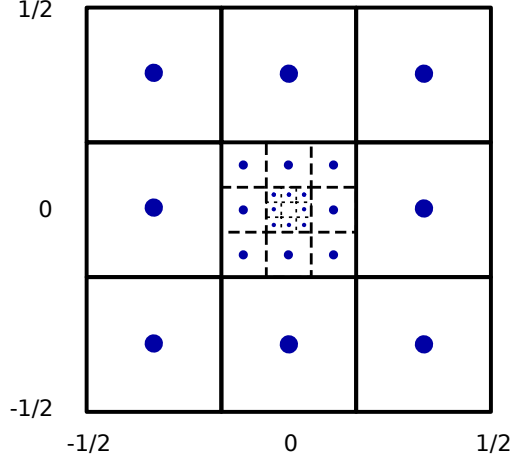


Fig. 14.— The generated set of subharmonic samples for three subharmonic sets. The squares indicate the area that each sample represents in the Fourier plane. The spacing of these samples is irregular, so these samples can't be Fourier transformed using the FFT algorithm.

spectrum of  $\phi_{\text{low,harm}}(\mathbf{r})$  is given by the scaling relation of Equation 55:

$$|\Phi_{\text{low,harm}}(\mathbf{k})| = \left| \frac{1}{\beta} \Phi_{\text{low}}\left(\frac{\mathbf{k}}{\beta}\right) \right| = \beta^{\frac{5}{6}} |\Phi_{\text{low}}(\mathbf{k})| \quad (62)$$

Another thing to look out for is sampling the same spatial frequencies twice: both by  $\phi_{\text{low,harm}}(\mathbf{r})$  and  $\phi_{\text{FFT}}(\mathbf{r})$ . This can be avoided by removing some Fourier samples from  $\Phi_{\text{FFT}}(\mathbf{k})$  and let those samples be sampled by  $\Phi_{\text{low,harm}}(\mathbf{k})$ . This is equivalent to setting a square of  $1/\beta \times 1/\beta$  the size of the spectrum matrix, centered around the zero-frequency sample, to zero. This whole algorithm is described diagrammatically in Figure 15.

We generally measure the performance of phase screen generation algorithms by looking at the average phase structure function of the generated phase screens. In Figure 16 we can see the phase structure functions for increasing factor  $\beta$ , along with the theoretical Kolmogorov phase structure function. The  $1024 \times 1024$  phase screens were generated with increasing  $\beta$  and  $1024 \times 1024$  harmonic, correcting phase screen, leading to an effective outer scale of about  $\beta$  times the size of the phase screens. We can see that the phase structure function is increasingly better with increasing  $\beta$ . This is expected due to the increase in the outer length scale.

This algorithm can be adapted to work with arbitrary spectra (e.g. Von Kármán) but this path hasn't been explored. Our algorithm can also be seen as using a crude adaptive Fourier transform algorithm, which puts more samples where the spectrum changes the most. Our method can therefore also be expanded by using more than two layers, although adding too many layers may be a disadvantage.

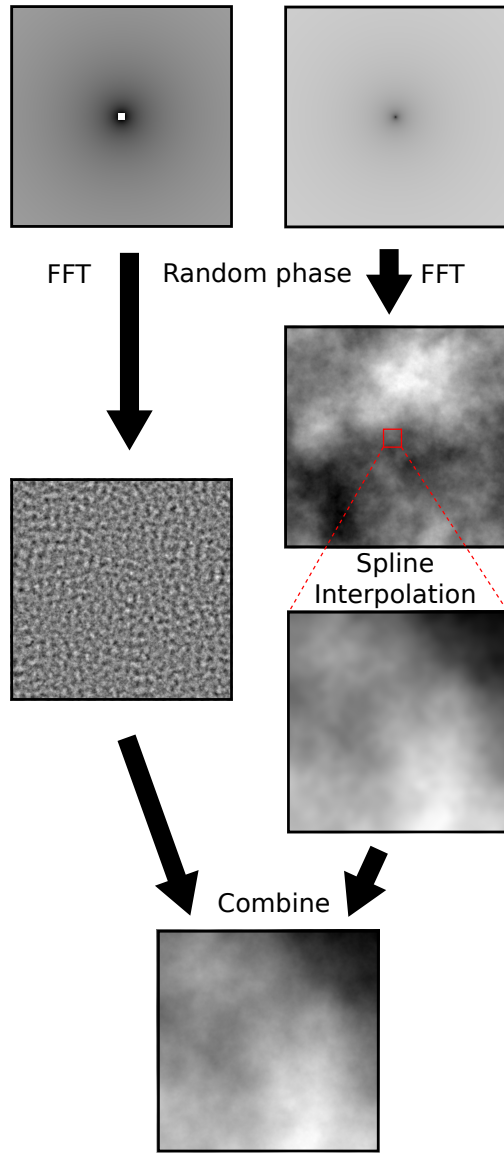


Fig. 15.— A diagram of the generation of our phase screens. The spectra are log-scaled. All colourscales are from white→black, low→high. The pure-white square in the center of the left phase screen spectrum is zero. The right phase screen is upsampled and added to the left phase screen to form the final phase screen.

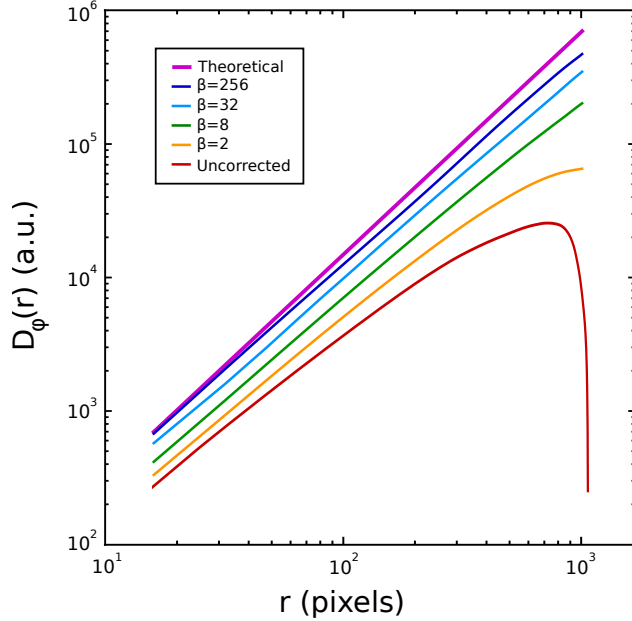


Fig. 16.— The average phase structure functions generated by our algorithm with increasing  $\beta$ . Also plotted are the theoretical and the uncorrected phase structure functions. We can see that the algorithm performs better with larger  $\beta$ .

#### 4.5. Time dependence

As the atmosphere itself isn't stationary, the phase screens are also time-dependent. We can simulate this effect using the model of multiple turbulent layers that each act as a phase screen on the incoming light. This model has the advantage that it mimics the physical process in the atmosphere, but it is computationally demanding. Additionally, we have to specify the velocity and direction of each layer, which increases the number of input parameters. As the atmosphere above Leiden has not been characterised yet, we decided to implement the time-dependence according to Glindemann et al. (1993).

They split the time-dependence into two parts: the shift of a rigid phase screen and the evolution of this phase screen with time. The first makes use of the approximation made by Taylor (1938): a phase screen at a later time can be approximated by the shifted version of the current wavefront if the lifetime of the turbulent cells  $\tau$  is much larger than the time interval between these two phase screens  $\Delta t \ll \tau$ . This shift is implemented as a phase shift in the Fourier plane:

$$\Phi_{\text{shift}}(k, \ell) = \Phi_{\text{old}}(k, \ell) \exp \left( 2\pi i \left[ \frac{kN_s}{N} + \frac{\ell M_s}{M} \right] \right), \quad (63)$$

where  $\Phi_{\text{shift}}(k, \ell)$  is the spectrum of the shifted phase screen,  $\Phi_{\text{old}}(k, \ell)$  is the spectrum of the old phase screen,  $N_s, M_s \in \mathbb{R}$  are the number of pixels that the phase screen has shifted in the x- and y-direction respectively. Note that doing this in the Fourier plane allows us to shift by non-integer

values of  $N_s, M_s$ .

The second part that Glindemann et al. introduced is the so-called boiling of the atmosphere. This process simulated using a Markov-chain process. We can generate the spectrum of the new phase screen  $\Phi_{\text{new}}(k, \ell)$  by combining the spectrum of the shifted old phase screen  $\Phi_{\text{shift}}(k, \ell)$  with a second independent spectrum of a phase screen  $\Phi(k, \ell)$  as follows:

$$\Phi_{\text{new}}(k, \ell) = \frac{\Phi_{\text{shift}} + \alpha(k, \ell)\Phi(k, \ell)}{[1 + \alpha^2(k, \ell)]^{1/2}}, \quad (64)$$

where  $\alpha(k, \ell)$  is a decorrelation factor that affects the velocity of the evolving process. Glindemann et al. defined  $\alpha(k, \ell) = C \frac{2}{N} \sqrt{k^2 + \ell^2}$ , where  $C$  is the only parameter that describes the evolving process. This parameter depends on the timestep  $\Delta t$ .

#### 4.6. Normalisation

After the phase screens have been generated, they have to be normalised. This means that we can set the Fried-parameter of our phase screens to whatever value we want. For convinience, we'll set  $r_0 = 1$  pixel in the normalisation routine, so that we can set the real  $r_0$  value when we know the scale of the image (in m/pixel).

The usual way<sup>1</sup> of normalising a phase screen is by generating a seeing disk. This method involves generating many independent phase screens and looking at the image of a point source through these phase screens. All those images are added together to form a seeing limited disk, similar to a long exposure image through an atmosphere. We can then find the Full Width Half Maximum (FWHM) of this seeing disk as a function of the normalisation factor. These points are then fitted to the theoretical FWHM:

$$\text{FWHM}(x|\alpha) = \sqrt{(\text{FWHM}_{\text{diff}})^2 + (\alpha x^{\frac{6}{5}})^2}, \quad (65)$$

where  $\text{FWHM}_{\text{diff}} = 1.029 \frac{\lambda}{D}$  is the diffraction limited FWHM, and  $\alpha$  the fit parameter. We can then find the correct normalisation factor  $\hat{x}$  by comparing this to the theoretical FWHM of the seeing disk at the specified input parameter  $\lambda/r_0$ :

$$\hat{x} = \left( \frac{\text{FWHM}_{\text{seeing}}}{\hat{\alpha}} \right)^{\frac{5}{6}}, \quad (66)$$

where  $\text{FWHM}_{\text{seeing}} = 0.98 \frac{\lambda}{r_0}$  is the theoretical seeing limited FWHM, and  $\hat{\alpha}$  the estimated fit parameter  $\alpha$ . In Figure 17 we can see such a seeing limited disk after 1000 realisations of the atmosphere, together with its radial density. In Figure 18 we can see the sampled normalisation factors with the fit and the correct normalisation factor.

---

<sup>1</sup>private communications: M. Kenworthy

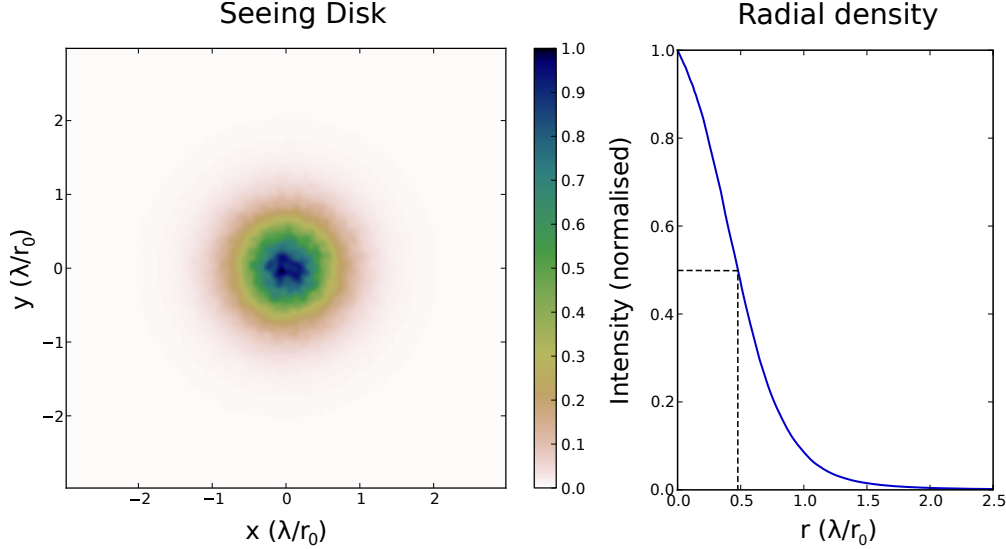


Fig. 17.— The simulated seeing limited disk at the correct normalisation factor for 1000 phase screen realisations. The intensity is normalised. The parameters were  $D = 30\text{ cm}$ ,  $r_0 = 3\text{ cm}$ , and  $\lambda = 500\text{ nm}$ . Although this isn't as clean as a real observation, its radial density is clean enough to obtain a reliable FWHM of the spot.

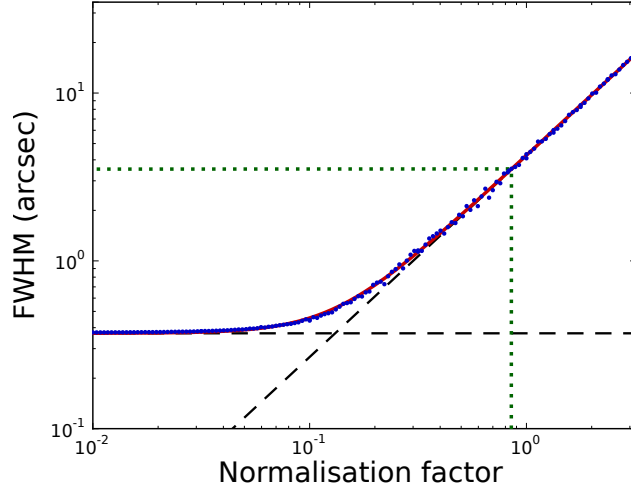


Fig. 18.— The FWHM as a function of the normalisation factor, along with the fitted function. The striped lines are the FWHM in the diffraction limited regime and in the seeing limited regime. The dotted line indicates the theoretical seeing limited values. The number of phase screen realisations was 1000 for normalisation factor larger than 1. Otherwise, only 500 realisations were used. The final normalisation factor turned out to be 0.830.

## 5. Implementation at Leiden Observatory

### 5.1. Student telescope

For our implementation of SAM, we used the Student Telescope located in the West Koepel at the Leiden Old Observatory, which was installed in 2012. The dome of this telescope is manually operated, which means that during exposures the dome has to be tracked by hand. The telescope is mounted on a high pier, which houses all power and network connections. The telescope consists of:

- The telescope mount: *Software Bisque Paramount ME*. This mount is a German Equatorial Mount (GEM) and is computer controlled using *TheSkyX*.
- The optical tube: *Takahashi Mewlon 300*. This is a Dall-Kirkham (Cassegrain) style telescope with a 300 mm diameter aperture, with 32% secondary obscuration.
- The optical manifold: *Van Slyke Instruments SideWinder Optical Manifold*. This allows attaching multiple instruments to the telescope and switching between these instruments.
- The slow camera: *FLI Proline 16803 CCD Camera*. This camera is used for telescope pointing and alignment.
- The fast camera: *The Imaging Source DMK 21AU618.AS*. This camera supports up to 60 frames per second with a  $640 \times 480$  pixel CCD. It has a read-out-noise of  $5e^-$  standard deviation and a variable gain. The program **FireCapture** was used to take the data. The raw data shows a lower cutoff at 0, producing a cutoff normal distribution as the read-out noise. This non-normal distribution becomes a serious problem when reducing the data.

Being a Dall-Kirkham design telescope, the optical system does exhibit off-axis coma. This coma may increase the errors on the closure phases measurements if its also visible within one sub-aperture, but this did not prove to be a limiting factor.

### 5.2. Field expander and filters

The telescope has a native resolution with the fast camera of 0.33 arcsec/pixel. However, the highest frequency fringes have a period of  $\frac{500\text{ nm}}{270\text{ mm}} = 0.38$  arcsec. Because we need sampling of the highest frequency fringes with at least 4 pixels, we expand the platescale with a magnification of  $\sim 4$ . This is typically done by using a Barlow lens, a negative lens placed before the focal plane of the telescope. The setup is displayed schematically in Figure 19.

The choice of the lens was made using two criteria <sup>2</sup>. The size of the beam on the lens should

---

<sup>2</sup>private communications: R. Stuik

## Beam Expander

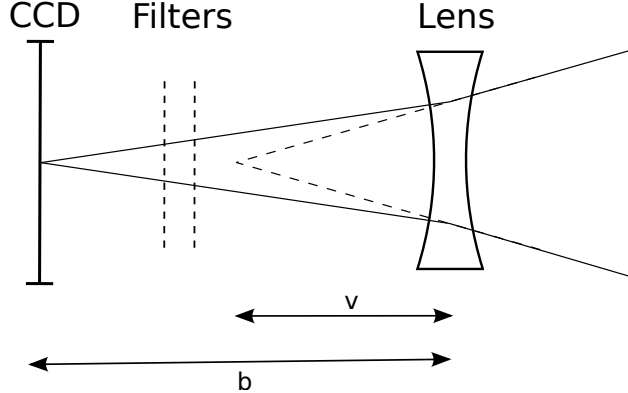


Fig. 19.— A schematic view of the field expander. We can see the CCD, two filters and the lens. The field expander magnifies the field by a factor  $N = b/v$ . This figure is not to scale.

be minimised in order to reduce lens aberrations, and the total system length should be minimised for practical reasons. The chosen lens is the ACN127-020-A lens from Thorlabs. This lens has a focal length of 20 mm and diameter 12.7 mm resulting in a diameter of the beam on the lens of  $\sim 1.3$  mm.

Inside the lens assembly of the beam expander there is room for two filters (for long- and shortpass filters). The mechanical design is available from R. Stuik upon request.

### 5.3. Mask and mask holder

The mask holder is a plastic ring directly screwed into the hood of the telescope. This ring accomodates four clips that hold the mask in place, and four alignment pins positioned above the secondary mirror support structure for use as a reference point when making the mask. These pins serve the purpose of keeping the mask orientation constant with respect to the telescope tube, and therefore the sky.

The mask is laser-cut out of 1 mm thick black, opaque plastic. The resolution of the laser printer is sufficient for our purpose. Measuring the hole distances of the created mask by hand did not show significant distortion of the baseline lengths. The laser printer was limited by a maximum size of 298 mm. Therefore the mask itself had a diameter of the same length. The mask and mask holder is shown in Figure 20.

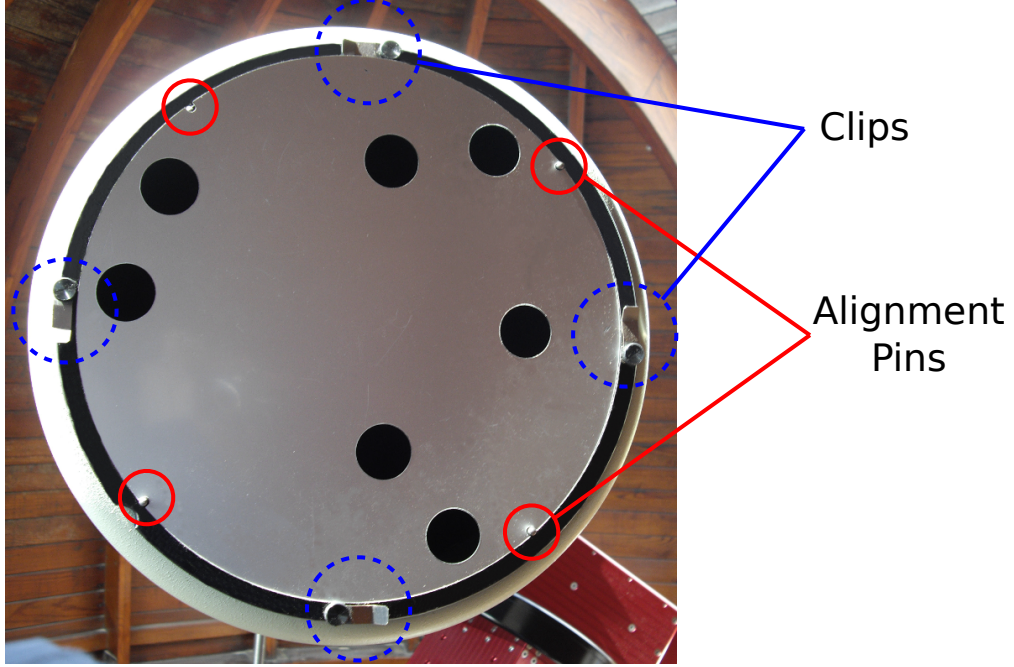


Fig. 20.— The mask holder with mask mounted onto the telescope. The mask is held in place by the four clips on the mask holder. The four alignment pins hold the mask in the correct orientation.

#### 5.4. Target choice

Possible targets were selected from the Washington Double Star Catalogue (WDS) using the following criteria:

- The separation must be between 0.2 and 1 arcsec, to be able to see the binary with the closure phases.
- The binary must be brighter than magnitude 4, a reasonable estimate given by crude simulations and earlier observations.
- The contrast ratio between the two stars must be smaller than 3 magnitudes.
- The star must be visible from Leiden.

These three criteria greatly reduced the search space and left only  $\sim 20$  candidate targets. The star  $\alpha$  UMa was chosen as our binary target for its convenient location on the sky at the time of observation. The star  $\alpha$  Boo was chosen as our single, calibrator star for its high brightness, which reduces the needed integration time. Parameters of these two star are compiled in Table 2.

Star name	Primary Magnitude	Secondary Magnitude	Separation
$\alpha$ Boo	-0.04	-	-
$\alpha$ UMa	2.02	4.95	0.6 arcsec

Table 2: The parameters for the observed targets.

### 5.5. Observations

Observations were carried out on the night of the 3rd to 4th of May 2013. Flatfields and dark frames were taken on the 27th of April 2013. The atmosphere was exceptionally stable, which was visually estimated from the data. Alignment on the stars were taken on the slow camera and then transferred to the fast camera. All data was taken with a 200 nm bandpass filter, ranging from 500 nm to 700 nm. A compilation of the observing log is shown in Table 3. During observing the telescope drift restricted the continuous exposure time to  $\sim 10$  min. Therefore we needed many observations per star. Moving of the dome during observing did not have an effect on the final data, because of the short duration of the distortion and the short integration time.

A short guide for observing with SAM at the telescope can be found in Appendix A.

Time started	Target	Observation Type	# frames	Mask orientation	Integration time	Comment
16-04-2013 20:15	-	Flat	2815	-	15.1 ms	-
16-04-2013 20:17	-	Dark	2922	-	15.1 ms	-
03-05-2013 23:35	$\alpha$ Boo	Science	1178	0 deg	15.1 ms	Settings check
03-05-2013 23:36	$\alpha$ Boo	Science	10255	0 deg	15.1 ms	-
03-05-2013 23:40	$\alpha$ Boo	Science	11668	90 deg	15.1 ms	-
03-05-2013 23:46	$\alpha$ Boo	Orientation	503	90 deg	100 ms	-
03-05-2013 00:02	$\alpha$ UMa	Science	36872	90 deg	15.1 ms	-
03-05-2013 00:16	$\alpha$ UMa	Science	36054	90 deg	15.1 ms	-
03-05-2013 00:32	$\alpha$ UMa	Science	15226	90 deg	30 ms	Dome moved
03-05-2013 00:43	$\alpha$ UMa	Science	16053	90 deg	30 ms	-
03-05-2013 00:54	$\alpha$ UMa	Science	36133	90 deg	15.1 ms	-
03-05-2013 01:13	$\alpha$ UMa	Science	36055	0 deg	15.1 ms	-
03-05-2013 01:27	$\alpha$ UMa	Science	36061	0 deg	15.1 ms	-
03-05-2013 01:41	$\alpha$ UMa	Science	16019	0 deg	30 ms	Dome moved
03-05-2013 01:52	$\alpha$ UMa	Science	8027	0 deg	30 ms	-
03-05-2013 01:57	$\alpha$ UMa	Science	22710	0 deg	15.1 ms	-

Table 3: A compilation of the observing log for our final dataset. All data was taken using a 200 nm filter. No mask was used for the dark and flat frames. Airmasses for  $\alpha$  Boo was 1.3-1.22 and for  $\alpha$  UMa 1.08-1.20.

## 6. Data Reduction

The whole data-reduction was written in Python and is available from the corresponding author upon request<sup>3</sup>. A short manual for the pipeline can be found in Appendix B.

### 6.1. Quick data-reduction

When we carry out observations at the telescope, we can do a quick, preliminary data-reduction to see if the data has been observed correctly. This data-reduction does not take advantage of the non-redundant mask, but will show the quality of the data. It consists of two main parts: shift-and-add and power spectrum averaging.

Shift-and-add is a technique developed to counter the tip-tilt in the wavefront. Tip-tilt contributes up to 87% to the total power of atmospheric turbulence (Fried 1965; Noll 1976), so discarding this part greatly increases the resolution of our measurements. The technique operates by shifting each frame so that its brightest pixel is in the center of the image, and then adding all those frames together. This results in a partial reconstruction of the PSF with no phase-shifts. Note that this algorithm uses the brightest pixel in the image, and is therefore very sensitive to the SNR of the star. In Figure 21 we can see the result of Shift-And-Add on the calibrator observations.

Secondly, we can calculate the average power spectrum of the frames. This should result in the baseline coverage of the mask, as in Figure 10. We can see the typical average power spectrum in Figure 22. The radial blurring that we can see in these images is the result of the finite bandwidth used. This power spectrum may also uncover noise structure in the image. In our case, we have a vertical line of noise peaks, whose strength depends on the brightness of the star. The cause is most likely a memory-effect, when reading out the CCD. This effect was not confirmed, but does not cause noticeable problems in the rest of the data-reduction. We can also see the effect of temporal decorrelation, which is higher at larger baselines. This reduces the visibility amplitude further away from the center of this image.

### 6.2. Existing pipelines

Now that we have assessed the quality of our data, we can continue with the full data-reduction pipeline. There are two main, existing pipelines for this kind of data. The first is the Sydney pipeline, written in IDL and developed by Sydney University, Cornell University and Caltech from 2004 onwards (Tuthill et al. 2006). This pipeline uses the complex valued Fourier transform of each frame to obtain the visibility phase for each baseline. The second is the Sparse Aperture Mode Pipeline (SAMP) written in Yorick and developed from 2010 onward at the Observatoire de

---

<sup>3</sup>[por@strw.leidenuniv.nl](mailto:por@strw.leidenuniv.nl)

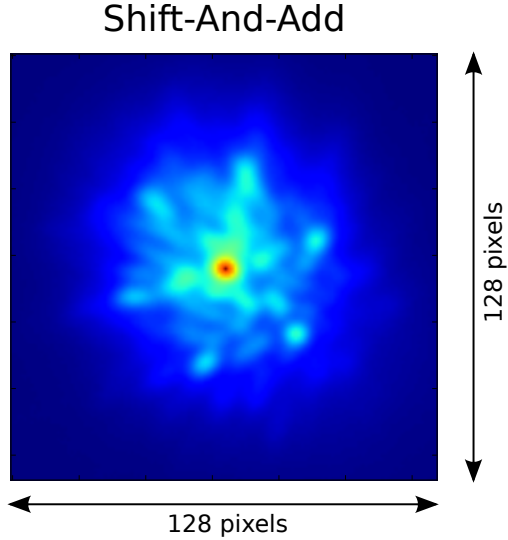


Fig. 21.— The image produced by Shift-And-Add on the calibrator (bright star) observations. We can see the 7 points in a hexagon with midpoint, just as in the PSF without phase-shifts in Figure 10.

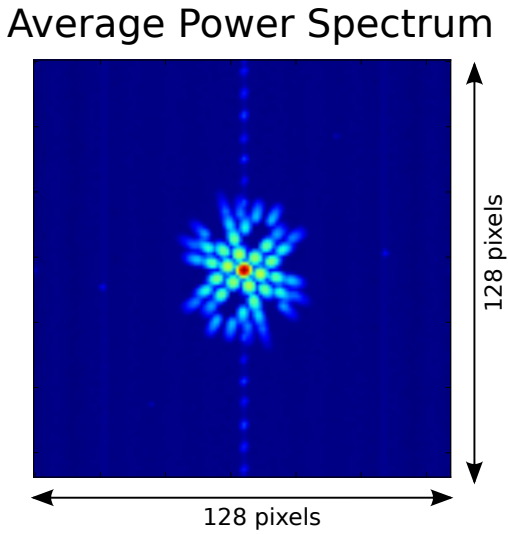


Fig. 22.— The average power spectrum of the calibrator observations. We can see the baseline coverage of the mask, bandwidth blurring, noise structure dependent on star strength and temporal decoherence at the larger baselines.

Paris (Tuthill et al. 2010a; Lacour et al. 2011a). This pipeline uses least square fringe fitting on each frame to obtain the visibility phases. These two pipelines have been cross-checked numerous times.

Both algorithms show the same general structure:

- *Pre-reduction.* The data is flatfielded, bad-pixel corrected and background-subtracted.
- *Complex visibility.* The complex visibilities are extracted from each frame.
- *Bispectrum.* The bispectra are obtained for each of the frames and are combined to give us the closure phase for each of the closure triangles in the mask.
- *Calibration.* The closure phases obtained on the calibrator are fitted with a polynomial function in the time-domain and subtracted from the science object. The closure phases change in time because the telescope primary mirror flexes slightly under its own gravity for different pointings.
- *Detection.* The corrected closure phases are fitted to a model of the science object. Various parameters can be estimated from the  $\chi^2$ -map. Binary star models are mostly used in this step.

If the star is faint, the Fourier transform (as used by the Sydney Pipeline) is swamped by the read-out noise. We also have to average over the splodges in the Fourier transform without introducing bias in the result. Additionally we have to filter out the noise far away from the star using a window function. The shape of this window function directly influences the phase and amplitude of the Fourier transform, which makes further analysis more difficult.

We therefore chose to use a data-reduction structure similar to the SAMP pipeline. Several things can be simplified, due to a different telescope size and data acquisition method. We'll describe the different parts of the data-reduction in more detail. A short manual for the data-reduction pipeline can be found in Appendix B.

### 6.3. Pre-reduction

All imaging that are reduced are dark-subtracted and flatfield-corrected. Bad-pixel correction has not been implemented, because our camera doesn't have any. There are a few hot pixels, which in particular show up in long ( $> 0.5$  second) exposures. These are corrected for by the dark frames. The read-out noise did not show any recurring pattern, as followed from the average power spectrum of all dark-frames.

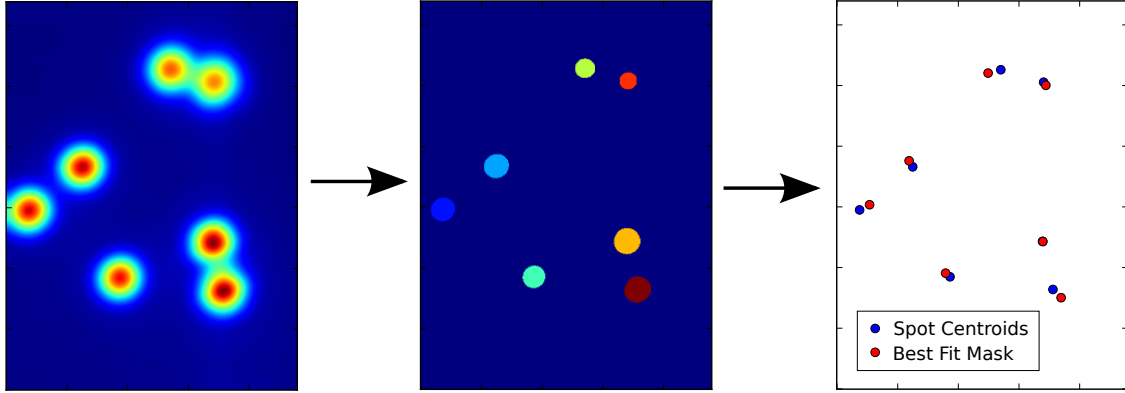


Fig. 23.— Determining mask orientation. All frames are added together and convolved with a Gaussian (left). Each spot is extracted from the image (middle) and the centroids are fitted to the mask hole positions (right).

#### 6.4. Mask orientation and pixel scale

When making an out of focus observation, the wavefront picks up an additional phase, best described with the defocus Zernike polynomial (second order, zero frequency)  $Z_4(\rho)$ :

$$Z_4(\rho) = \sqrt{3}(2\rho^2 - 1). \quad (67)$$

As this polynomial is quadratic in  $\rho$  (the radial distance to the optical axis), the tip-tilt at a given position varies linearly with  $\rho$ , and therefore, when we image a point-source out of focus, we get a undistorted image of our aperture. This assumes that other Zernike polynomials (except for piston, tip or tilt) can be neglected. If this is not the case, the orientation resulting from this method may be biased.

The raw frames are all dark-corrected and flatfielded, and added together. The result is shown in Figure 23. We convolve this image with a small Gaussian kernel, to make it easier to find the centroid of each spot. We then threshold the image, lowering the threshold until all mask hole spots are visible. Then the centroid of each spot is found and these are fitted to the mask. The scale and position of the mask is irrelevant as it depends on telescope pointing and the out of focus distance. The orientation is then applied to all observations within a block bounded by a filter change (for which the lens holder needs to be detached, destroying all orientation information). We can see this whole process diagrammatically in Figure 23.

We also need to find the pixel scale of our detector. This is normally done by observing a known field and fitting the resulting image to a catalogue. We can do a similar thing by observing a well-known, wide binary that still fits onto our detector. These observations can be done with a longer integration time, and without an aperture-mask. In our observations, the pixel scale was manually estimated from the shift-and-add images. This proved sufficient for this data-reduction.

## 6.5. Star centering

Finding the center of the star is very important for correctly fitting the fringes. Errors in finding the center of the star results in reduced fringe visibility and therefore increased error in the visibility phase. For faint stars we need to bin the pixels to reach high certainty in the centroid of the star. We therefore convolve each frame with a Gaussian kernel with a standard deviation  $\sigma$  equal to that of the Gaussian approximation of the Airy disk:

$$\sigma \approx 0.45\lambda/d, \quad (68)$$

where  $d$  is the hole diameter and  $\sigma$  is in radians. This width ensures a sharp peaked function after the convolution. The center of the star can then be easily found by the maximum of the resulting function. All but a small part of the frame around the center of the star is discarded, for computational efficiency.

## 6.6. Fringe fitting

The data is windowed to reduce the influence of noise far away from the star. Sharp cut-offs as well as non-circularity of the window-function negatively influence the fringe fitting results. The exact choice of windows doesn't matter as much: it mimics the weights used in the least squares fit that we will do and therefore should be similar to the SNR that we expect on each pixel. We therefore decided to use the two-dimensional second order super-Gaussian:

$$f_{\text{window}}(\mathbf{r}) = e^{-|\mathbf{r}|^4/w^4}, \quad (69)$$

where  $w$  is the waist of the super-Gaussian. We can see this function with a Gaussian function in Figure 24. In Figure 25 we can see the process of windowing a typical frame of a bright star.

Now we are ready to do a least square fit of each frame. The SAMP pipeline carries out a numerical non-linear least square (NLLS) fit using the Levenberg-Marquardt algorithm<sup>4</sup>. Their fit includes a few parameters that we have estimated beforehand, such as wavelength, detector orientation and hole diameter. These parameters make their fit-function non-linear, which forces them to perform the least squares fit numerically. Our fit-function is purely linear, which allows us to do an analytical linear least squares (LLS) fit. For each fringe there are two parameters we need to estimate. For the zero-frequency slodge we only need to estimate one, which brings the number of free parameters to  $2n_{\text{vis}} + 1 = n_{\text{holes}}(n_{\text{holes}} - 1) + 1$ , for  $n_{\text{vis}}$  the number of visibility fringes and  $n_{\text{holes}}$  the number of holes.

We have chosen to fit the real and complex part of visibilities as separate functions instead of amplitude and phase, for numerical stability resulting from the scale similarity in the parameters. Some of the linear parts of the fit-function are shown in Figure 26.

---

<sup>4</sup>private communication: S. Lacour

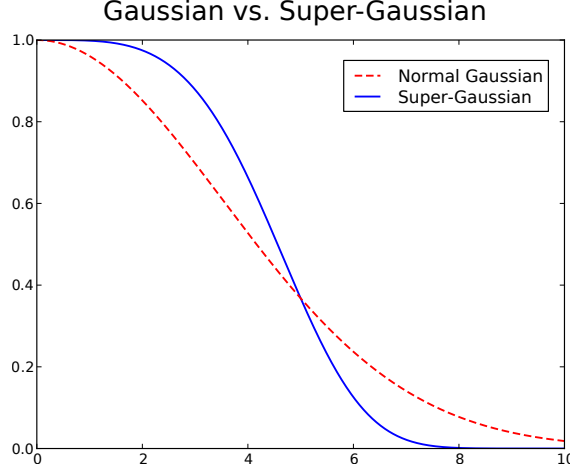


Fig. 24.— A super-Gaussian compared to a normal Gaussian. We can see that the super-Gaussian falls off more quickly, but is still smooth and goes to  $\sim 0$  at the edge, compared to the normal Gaussian, avoiding edge effects.

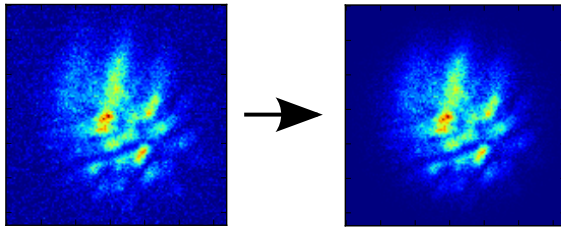


Fig. 25.— Here we can see the process of windowing for a typical fringe frame of a bright star. The windowing ensures that we only fit the high SNR part of the fringes and ignore the noise parts on the edge of this frame-cut-out.

Using an analytical linear least squares fit, the whole fitting problem reduces to a single matrix-vector multiplication, as we saw in Section sec:linearleastsquares. An analytical expression allows for a much faster data-reduction compared to numerical optimisation of the sum-of-squares. In our implementation, it allowed for  $\sim 70\times$  increase in frame analysis speed, which reduced the data-reduction time of one night of observations from one month to about half a day on a typical desktop computer. In Figure 27 we can see a typical windowed frame together with its best fit, the residuals and a histogram of those residuals.

### 6.7. Bispectrum and lucky imaging

We can calculate the bispectrum for each closure triangle on the mask for each frame by multiplying the correct visibilities. The argument of the bispectrum gives us the closure phase, of which the error is calculated using the error on the visibilities. We can see the visibility angle for

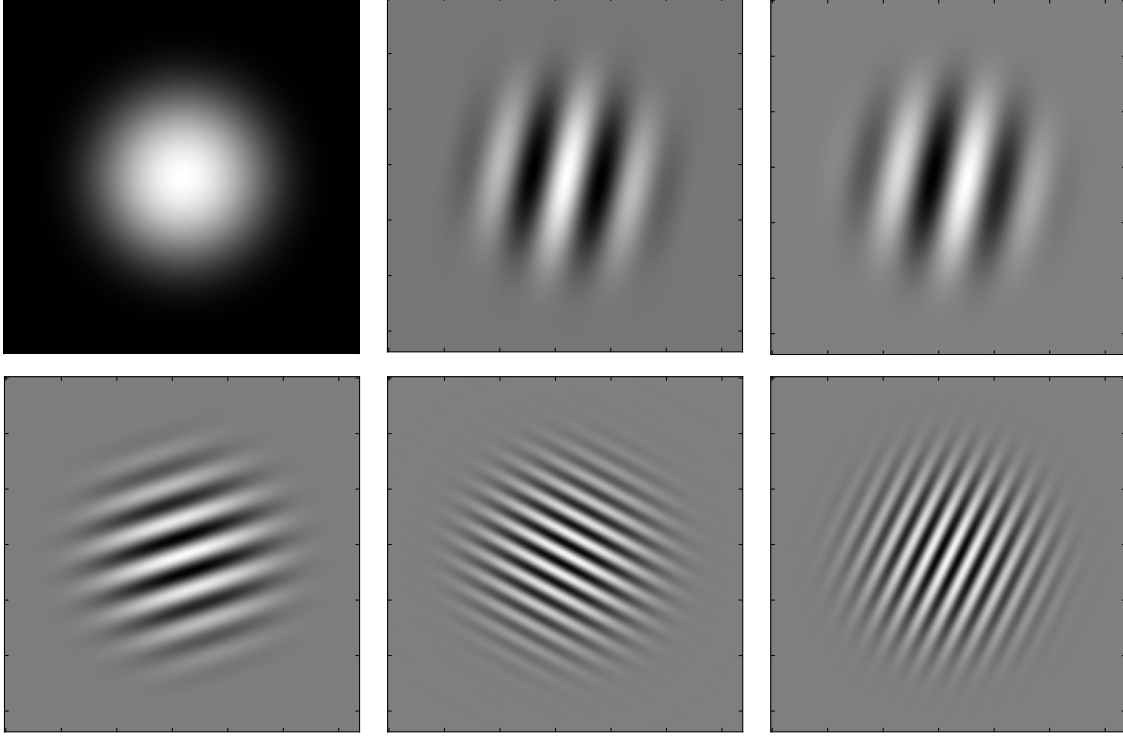


Fig. 26.— Some of the linear parts of the fit-function. The final fit-function is a linear combination of all these functions. We can see the zero-frequency function, the sine and cosine functions of a low-frequency fringe and a few more fringes in different directions and frequencies. All these functions are derived directly from the mask and observed mask orientation.

three baselines constituting a closure triangle for 50 consecutive frames of a calibrator (a single and bright star) and the corresponding closure phase in Figure 28.

The resulting values for both calibrator and binary star are analysed in Figure 29. We can also see if there is a correlation between the error on the closure phase and the closure phase itself, when we plot those as in Figure 30.

When the error and the value are correlated, we can use an analogue of lucky imaging: we discard all closure phases with an error higher than a specified value. In our case we only used the 10% best measured closure phases. This threshold is rather arbitrary, but determining the best threshold falls outside of the scope of our project. A programming bug or numerical error discovered late in the project, the binary closure phase errors were altered, making it impossible to use lucky imaging. The source of this problem was found and eliminated. Due to time constraints the pipeline wasn't run again, which means that the results in the rest of this section don't use the binary closure phase errors. The difference in using the binary closure phase errors is deemed minimal, but noticeable.

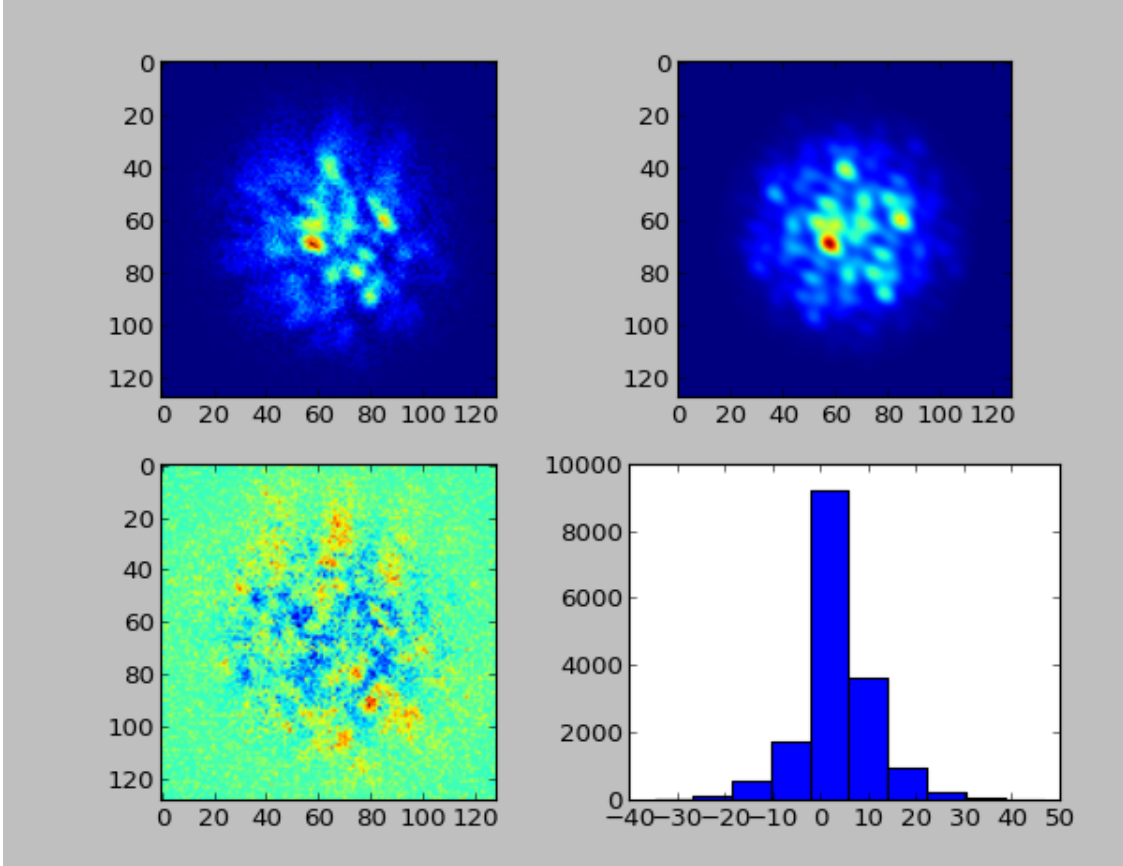


Fig. 27.— A typical figure from the data-reduction pipeline during the actual fringe fitting. We can see the windowed star (upper left) and its best fitting theoretical function (upper right). We can see some structure in its residuals (lower left) but there is no real fringe structure visible. A histogram of these residuals is also shown (lower right). Note that this is just a single frame in the whole data-reduction.

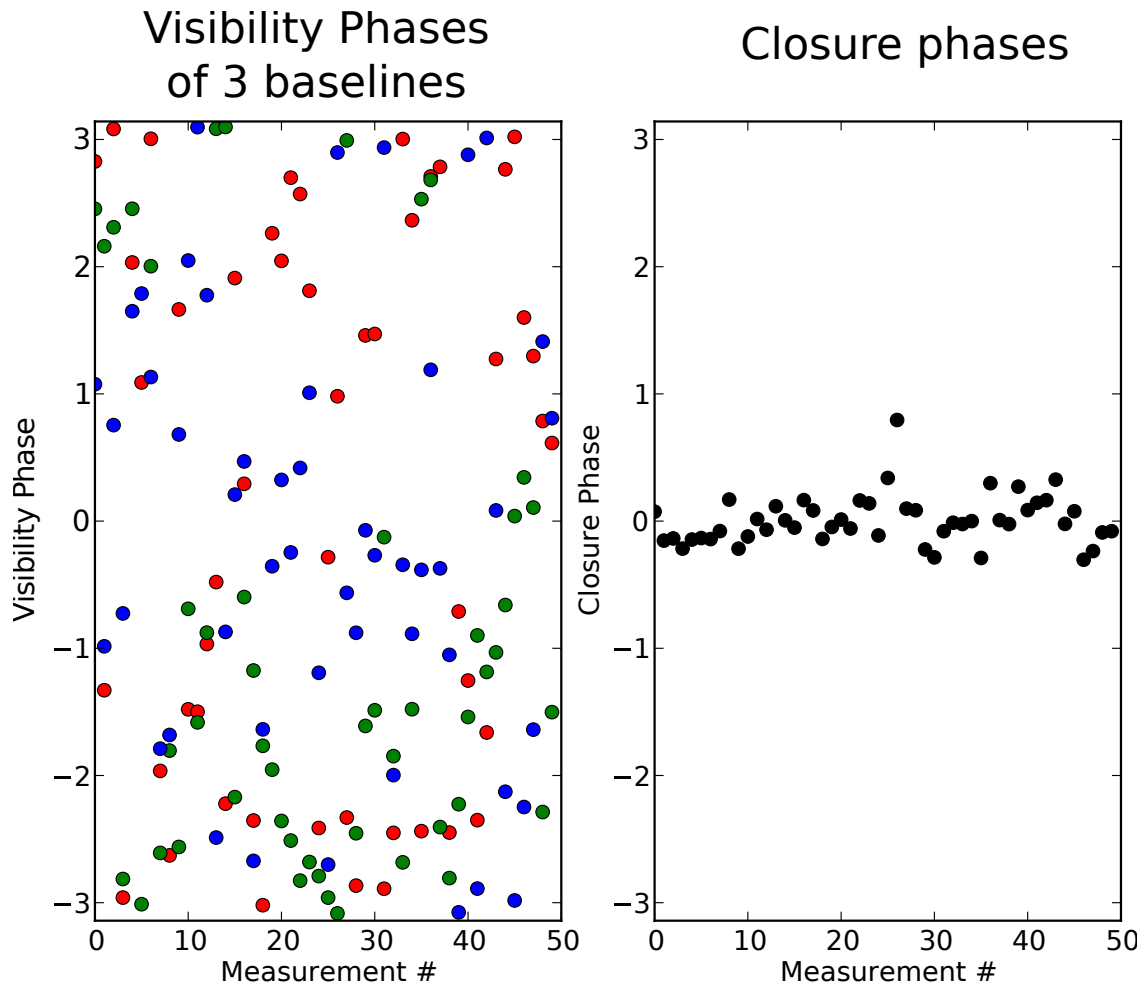


Fig. 28.— The visibility angles for three baselines constituting a closure triangle (left) and the corresponding closure phase (right). The data points are 50 consecutive frames of a calibrator observation. We can see that the variance of the closure phase is much smaller than that of the visibility phases.

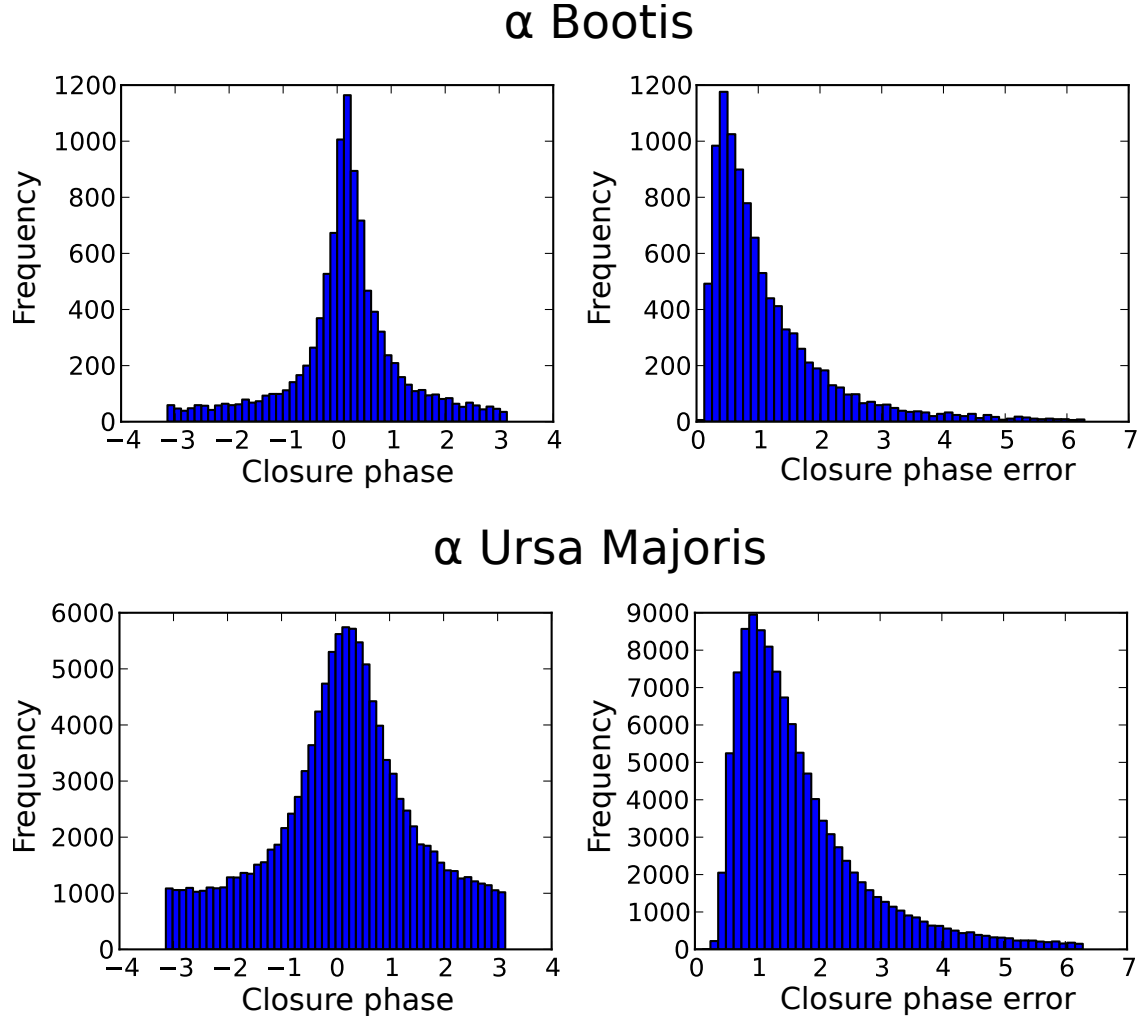


Fig. 29.— Histograms of measured closure phases for *one* typical closure triangle, for the calibrator star (upper left) and the binary (lower left), and its error (upper right and lower right). We can see that the closure phase histogram for the calibrator has a well defined peak, but has big tails compared to a theoretical wrapped normal distribution. The closure phase histogram shows the same features, however it is much broader and wider. The closure phase error histograms have the same general shape for the single and the binary star, but the binary closure phase errors are larger, resulting in a broader peak in the closure phase histogram. The cause for the larger closure phase error can be entirely attributed to the reduced brightness of the binary compared to the single star, see 2.

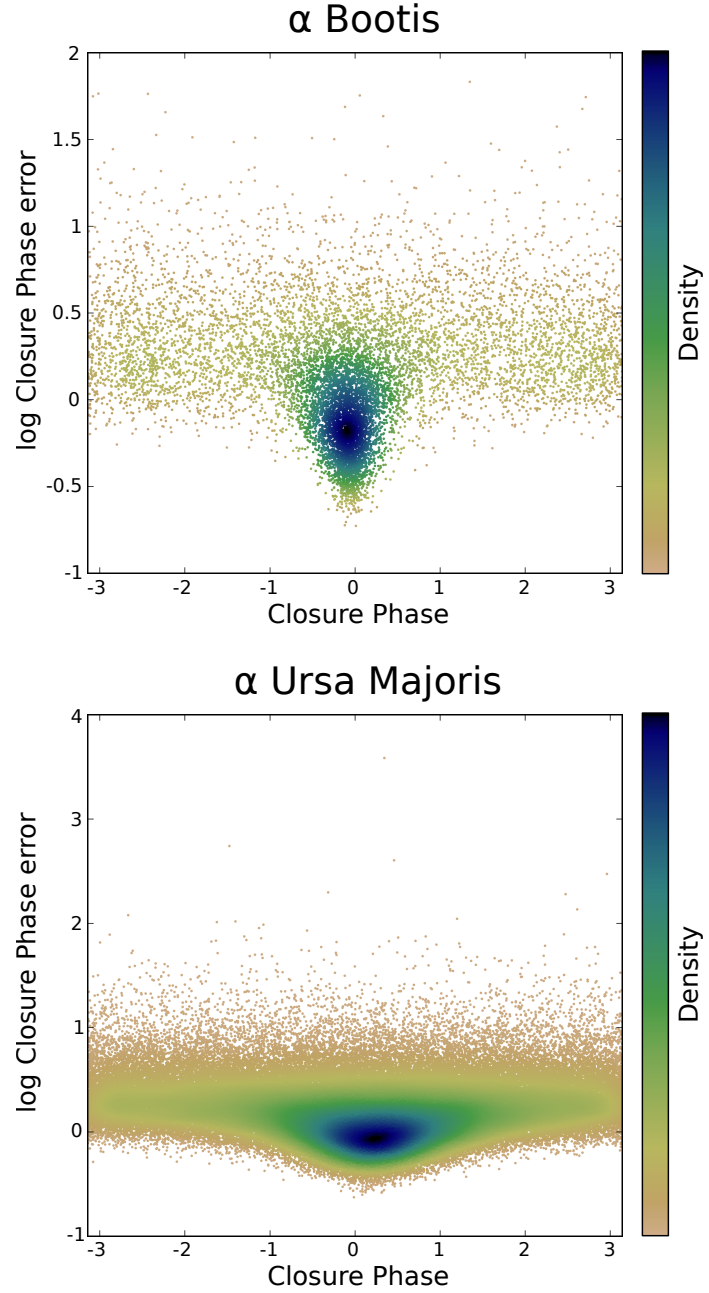


Fig. 30.— A plot of the closure phase error versus the closure phase for the calibrator (top) and the binary (bottom) for a typical closure triangle. For the calibrator, we can clearly see a correlation between error and closure phase: the spread of the points around the mean increases with increasing closure phase error. The binary shows the same distribution, with much more data points and more emphasis at higher closure phase errors, as we saw in Figure 29. The colour scale is a measure for the density of the data points.

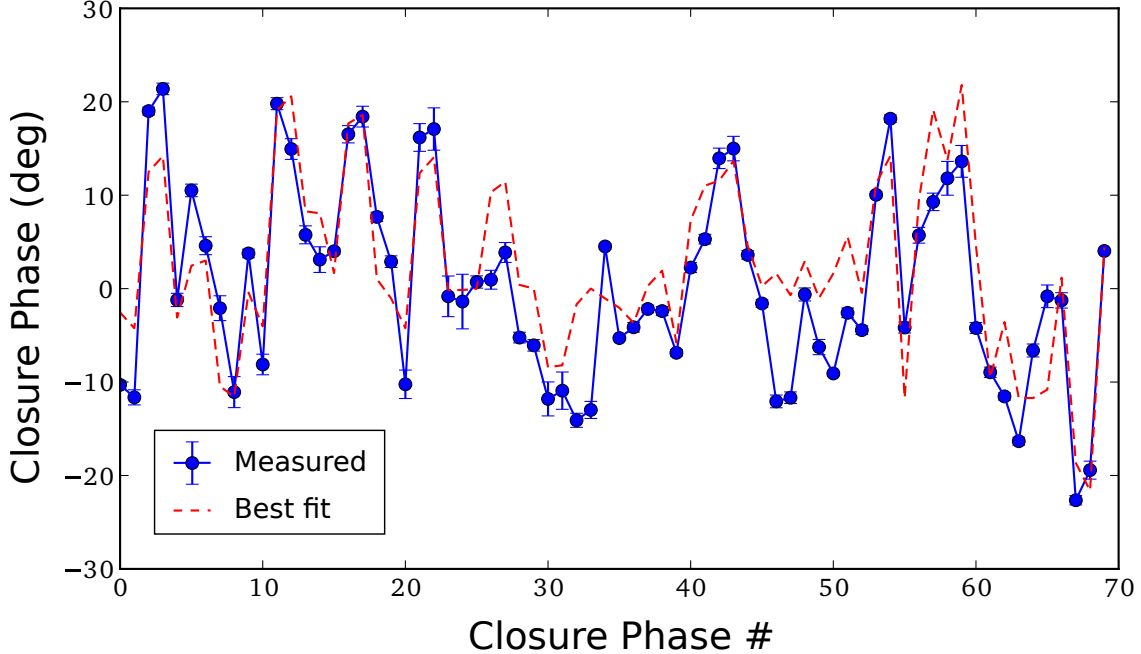


Fig. 31.— The calibrated closure phases of the binary with the best binary fit overplotted. The binary doesn't fit very well, but significantly better than a single star. This is due to the systematic errors in the data, mostly concerning the large bandwidth of these observations. The closure phases are ordered arbitrarily.

We proceeded to fit the average closure phase using maximum likelihood fitting, as described in Section 2.5. The error on the average closure phase was calculated using bootstrap. The end result of this section is a list of averaged closure phases for each closure triangle with corresponding errors.

### 6.8. Binary parameter estimation

When we got the average closure phase for each closure triangle we need to fit those to the binary. We subtract the calibrator closure phases from the binary closure phases to correct for systematic errors. We fit both orientations of the mask at the same time to increase detection probability. The fit is done using non-linear least squares, as described in Section 2.6. The closure phases with the fitted closure phases are shown in Figure 31. The  $\chi^2$ -map is shown in Figure 32. The results of the fit are shown in Table 4. The errors were determined using bootstrap of the distribution of  $F$  under the null-hypothesis. The contrast limits are shown in Figure 33. In these contrast limits, the systematic errors are treated as stochastic errors.

Parameter	Best Fit	$3\sigma$ confidence
Separation	0.33 arcsec	$0.25 \text{ arcsec} <  \rho  < 0.50 \text{ arcsec}$
Contrast ratio	0.15	$0.05 < r < 0.73$
$F$ -value	42	-
Significance	$\sim 5.5\sigma$	-
Reduced $\chi^2$	99.1	-
Average Closure Phase Error	$0.86^\circ$	-

Table 4: The resulting parameters of the binary fit, with  $3\sigma$  confidence intervals for some of the parameters. Although the binary model is a bad fit, as can be seen in the reduced  $\chi^2$  value, it still fits significantly better than the single star model, as seen in the  $F$ -value and the significance. The position angle could not be calculated, due to a lack of calibration of the mask orientation with respect to the sky.

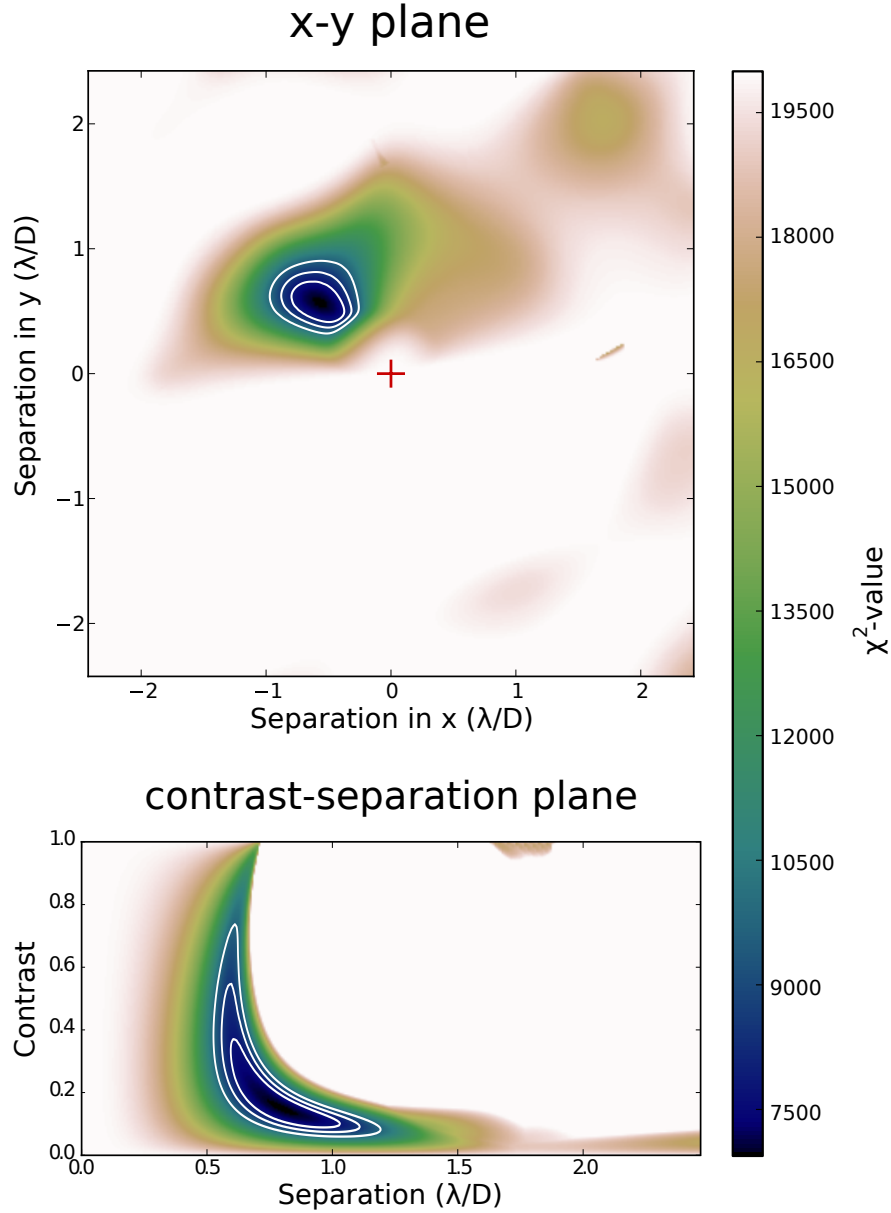


Fig. 32.— The  $\chi^2$ -map of the observed binary, projected onto the x-y plane and on the contrast-separation plane. We can see a very clear minimum. The three contours are the  $1$ ,  $2$ , and  $3\sigma$ -contours, in increasing order outward. The center cross is the primary star. We can see that the separation and contrast are strongly correlated.

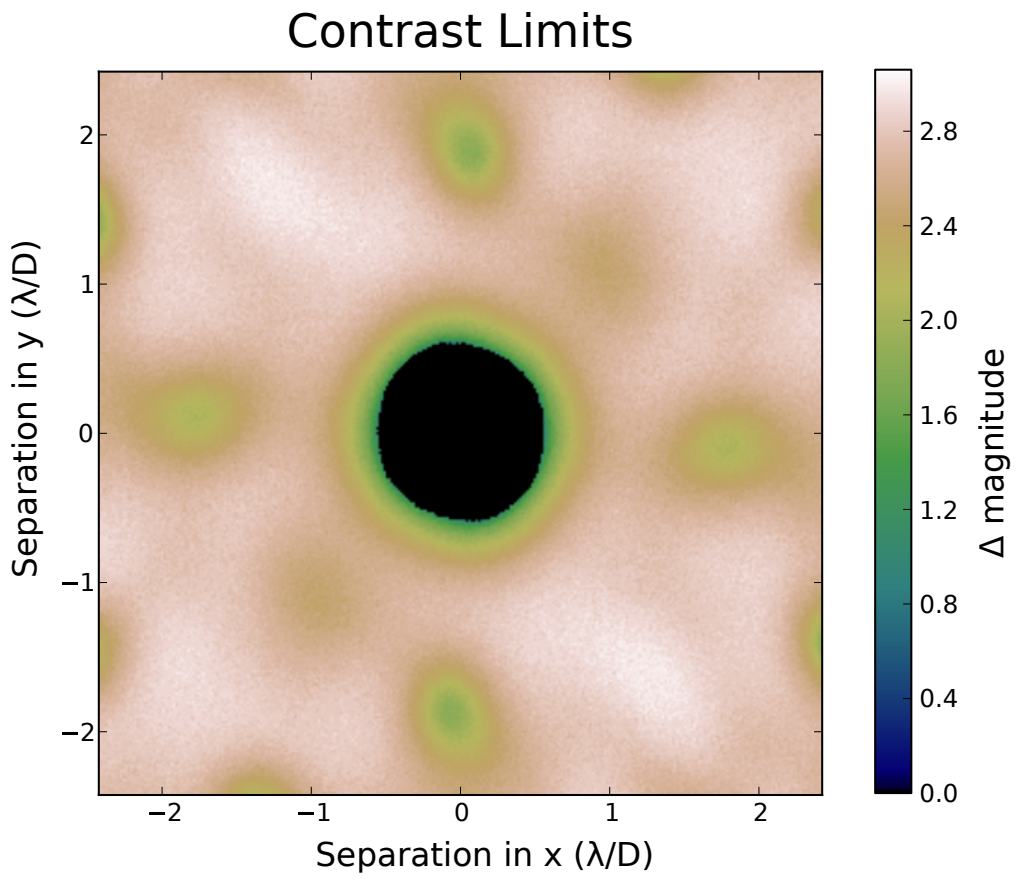


Fig. 33.— The  $3\sigma$  contrast limits of our data in magnitudes. The maximum contrast is limited by the systematic errors. We can see that we probed down to 2.5 magnitudes of contrast up to  $0.7\lambda/D$  with some small exceptions at certain position angles.

## 7. Conclusion and future work

### 7.1. Conclusion

We have implemented a Sparse Aperture Masking observing mode at the student telescope at the Leiden Old Observatory. The aperture mask was designed for binary detection at every position angle and separations from 1 arcsec to 0.2 arcsec. This mask, laser cut out of plastic, was held in front of the primary mirror by the mask holder, a plastic ring with clips that hold the mask in place and alignment pins that allow the mask to rotate only by 90°. A field expander was installed to sample of the highest frequency fringes. Observations were done of  $\alpha$  Boo, a single star, and  $\alpha$  UMa, a close binary star with a separation of 0.6 arcsec.

A data-reduction pipeline was written in Python, based on the SAMP pipeline. This pipeline flatfields, dark-corrects and windows the data. It then proceeds to fit the visibility fringes created by the mask using linear least squares. Closure phases are calculated from these visibilities, and averaged over all frames. The averaged closure phases are then fitted to a binary model. A  $\chi^2$ -map and the contrast limits are calculated and plotted (see Figures 32 and 33). The significance is determined using an empirical F-test, of which the critical values were calculated using bootstrap.

For our observations systematic errors still dominated the total error. Despite this a binary was found in our data at  $\sim 5.5\sigma$  confidence. The contrast limits showed that we can probe down to 2.5 magnitudes contrast up to  $0.7\lambda/D$  with a 2 magnitude primary star and  $\sim 1$  hour of effective integration time.

A new phase screen generation algorithm was created to correct for the lack of subharmonic frequencies in conventional phase screens, in a simpler way. These phase screens are used in simulations of SAM, which is integrated into the pipeline. Actual simulations were not used in this thesis.

### 7.2. Future work

There are still some improvements that can be made to the system to improve performance. First of all, additional masks could provide better performance than the current mask. Improvements in mask design are described at length in Section 3.5. In choosing the final mask, we could also make use of simulations to calculate the contrast limits plot, as this plot in the end determines our mask performance.

When using multiple masks, the optimal mask could be selected upon measurement of the Fried parameter at the time of the observation. These measurements could even be obtained without a seeing monitor, by using the mask as a multi-element H-DIMM, as described by [Bally et al. \(1996\)](#). A short integration time compared to the orientation measurements would be needed however.

The phase screen generation could be altered to use the Von Kármán spectrum instead. This

would generate more realistic phase screens, discussed in Floyd et al. (2010) and references therein.

Because the systematic errors dominate the stochastic errors, we need to reduce the former to reach a better performance. The reason for the large systematic errors is most likely the large bandwidth of the observations, but this is not clear. Further measurements with a reduced bandwidth are needed to be sure. In order to increase signal strength, we can also reduce the sampling of the detector. As can be seen in Figure 22 we are still oversampling the field. Even slight aliasing has been shown to work Tuthill et al. (2000). As we are read-noise limited, better sampling could decrease the closure phases errors up to a factor 3. Together, these changes would improve the reachable contrast by  $\sim 0.7$  magnitudes in the worst case and  $\sim 1.2$  magnitudes at best, assuming the error formulas in Ireland (2013).

## 8. Outlook

We now look at the recent developments in the field of SAM as a whole. An interesting development is, for example, the use of SAM in space. The JWST will have SAM implemented, as proposed by Sivaramakrishnan et al. (2010). Already being in space, NRM is not used to correct for atmospheric seeing, but only to go beyond the diffraction limit. Further simulations of system performance (Sivaramakrishnan et al. 2012) prove promising.

There are also several new techniques that are developed at this moment. These methods are mainly focused on overcoming the disadvantages of non-redundant masking. One main disadvantage is the short integration times that have to be used to freeze the atmosphere. Adaptive optics (AO) actively tracks and corrects the incoming wavefront with a wavefront sensor (WFS) and a deformable mirror (DM). The wavefront after an AO system allows for integration times of about a few minutes (Tuthill et al. 2006; Bernat 2012), a radical improvement over the few tens of a second that are used at telescopes without an AO system today (Tuthill et al. 2000).

An addition of this technique uses spatial filtering (Perrin et al. 2006; Lacour et al. 2007; Bernat et al. 2012) to reduce the residual wavefront error within one sub-aperture. The light from a sub-aperture is focused onto a single mode optical fiber. This flattens the wavefront, leaving only the tip-tilt error on the sub-aperture wavefront. This residual tip-tilt can be greatly reduced by the AO system.

Another main disadvantage is the loss of signal due to the mask itself. There are a few possible solutions for this problem. One of these is pupil remapping (Tuthill et al. 2010b). The light from the full pupil is remapped onto a non-redundant pupil. The main problem with this technique is that the guides that remap the light have to have the same length to within the coherence length of the light ( $\lambda^2/\Delta\lambda$ ). The guides therefore have to be on chip photonic circuits. This technique has already been tested with starlight (Jovanovic et al. 2012) in the infrared and provides a throughput of 55% to 65%, instead of the usual 5% to 10% of an aperture mask.

Another solution makes use of the low variance of the residual wavefront after an AO system: kernel phase interferometry ([Martinache 2010](#)). This technique discards the aperture mask altogether and therefore requires a very small wavefront phase variance (or high Strehl-ratio), which will be reached by extreme adaptive optics systems or space telescopes. This technique used closure phase like quantities (Ker-phases) between virtual sub-apertures. This also involves correcting for the redundancy in the visibilities. The technique has been successfully demonstrated on archive data acquired with the Hubble Space Telescope.

As each segment of a segmented mirror of a large telescope has about the right size for non-redundant masking, tilting the segments in such a way that multiple images are formed on the detector, which each have non-redundant baselines. This technique effectively increases the transmission of SAM and was first demonstrated on the Keck-I telescope ([Tuthill et al. 2000](#)). This observation mode was temporally unavailable, due to cancellation of a one needed instrument. It was tried again by [Monnier et al. \(2009\)](#) with good results and is now proposed for the JWST ([Sivaramakrishnan et al. 2012](#)).

## REFERENCES

- J. Bally, D. Theil, Y. Billawalla, D. Potter, R. Loewenstein, F. Mrozek, and J. Lloyd. “A Hartmann differential image motion monitor (H-DIMM) for atmospheric turbulence characterisation”. Publications of the Astronomical Society of Australia 13 (1996) 22–27.
- D. Bernat. *Non-Redundant Aperture Masking Interferometry With Adaptive Optics: Developing Higher Contrast Imaging To Test Brown Dwarf And Exoplanet Evolution Models*. Ph.D. thesis, Cornell University (2012).
- D. Bernat, F. Martinache, M. Ireland, P. Tuthill, and J. Lloyd. “The Use of Spatial Filtering with Aperture Masking Interferometry and Adaptive Optics”. The Astrophysical Journal 756 (2012), 1 8.
- A. Carlotti and T. Groff. “New approaches to the design of non-redundant aperture masks”. In *SPIE Astronomical Telescopes and Instrumentation: Observational Frontiers of Astronomy for the New Decade*, 77333D–77333D (International Society for Optics and Photonics, 2010).
- L. A. Cieza, S. Lacour, M. R. Schreiber, S. Casassus, A. Jordán, G. S. Mathews, H. Cánovas, F. Ménard, et al. “Sparse Aperture Masking Observations of the FL Cha Pre-transitional Disk”. The Astrophysical Journal Letters 762 (2013), 1 L12.
- S. Coles. “Inference for circular distributions and processes”. Statistics and Computing 8 (1998), 2 105–113.
- F. W. Diederich and J. A. Drischler. “Effect of spanwise variations in gust intensity on the lift due to atmospheric turbulence”. National Advisory Committee for Aeronautics (1957).
- D. J. Floyd, J. Thomas-Osip, and G. Prieto. “Seeing, Wind, and Outer Scale Effects on Image Quality at the Magellan Telescopes”. Publications of the Astronomical Society of the Pacific 122 (2010), 892 731–742.
- D. L. Fried. “Statistics of a geometric representation of wavefront distortion”. JOSA 55 (1965), 11 1427–1431.
- B. R. Frieden and W. Swindell. “Restored pictures of Ganymede, moon of Jupiter”. Science 191 (1976), 4233 1237–1241.
- A. Glindemann, R. Lane, and J. Dainty. “Simulation of time-evolving speckle patterns using Kolmogorov statistics”. Journal of modern optics 40 (1993), 12 2381–2388.
- J. Högbom. “Aperture synthesis with a non-regular distribution of interferometer baselines”. Astronomy and Astrophysics Supplement Series 15 (1974) 417.
- M. J. Ireland. “Detecting extrasolar planets with sparse aperture masking”. In *SPIE Astronomical Telescopes+ Instrumentation*, 844506–844506 (International Society for Optics and Photonics, 2012).

- M. J. Ireland. “Phase Errors in Diffraction-Limited Imaging: Contrast Limits for Sparse Aperture Masking”. arXiv preprint arXiv:13016205 (2013).
- R. Jennison. “A phase sensitive interferometer technique for the measurement of the Fourier transforms of spatial brightness distributions of small angular extent”. Monthly Notices of the Royal Astronomical Society 118 (1958) 276.
- N. Jovanovic, P. Tuthill, B. Norris, S. Gross, P. Stewart, N. Charles, S. Lacour, M. Ams, et al. “Starlight demonstration of the Dragonfly instrument: an integrated photonic pupil-remapping interferometer for high-contrast imaging”. Monthly Notices of the Royal Astronomical Society 427 (2012), 1 806–815.
- A. N. Kolmogorov. “The local structure of turbulence in incompressible viscous fluid for very large Reynolds numbers”. In *Dokl. Akad. Nauk SSSR*, vol. 30, 299–303 (1941). Reprinted in 1991.
- A. N. Kolmogorov. “The local structure of turbulence in incompressible viscous fluid for very large Reynolds numbers”. Proceedings of the Royal Society of London Series A: Mathematical and Physical Sciences 434 (1991), 1890 9–13. Reprint.
- A. L. Kraus and M. J. Ireland. “LKCA 15: A young exoplanet caught at formation?” The Astrophysical Journal 745 (2012), 1 5.
- S. Lacour, E. Thiébaut, and G. Perrin. “High dynamic range imaging with a single-mode pupil remapping system: a self-calibration algorithm for redundant interferometric arrays”. Monthly Notices of the Royal Astronomical Society 374 (2007), 3 832–846.
- S. Lacour, P. Tuthill, P. Amico, M. Ireland, D. Ehrenreich, N. Huelamo, and A. Lagrange. “Sparse aperture masking at the VLT”. Astronomy & Astrophysics 532 (2011a).
- S. Lacour, P. Tuthill, M. Ireland, P. Amico, and J. Girard. “Sparse aperture masking on Paranal”. The Messenger 146 (2011b) 18–23.
- R. Lane, A. Glindemann, and J. Dainty. “Simulation of a Kolmogorov phase screen”. Waves in random media 2 (1992), 3 209–224.
- F. Martinache. “Kernel Phase in Fizeau Interferometry”. The Astrophysical Journal 724 (2010), 1 464.
- B. L. McGlamery. “Computer simulation studies of compensation of turbulence degraded images”. In *Image processing*, 225–233 (International Society for Optics and Photonics, 1976).
- J. Monnier. “Phases in interferometry”. New Astronomy Reviews 51 (2007), 8 604–616.
- J. Monnier, P. Tuthill, M. Ireland, R. Cohen, A. Tannirkulam, and M. Perrin. “Mid-Infrared Size Survey of Young Stellar Objects: Description of Keck Segment-Tilting Experiment and Basic Results”. ApJ700 (2009) 491–505.

- R. J. Noll. “Zernike polynomials and atmospheric turbulence”. *J Opt Soc Am* 66 (1976), 3 207–211.
- G. Perrin, S. Lacour, J. Woillez, and E. Thiébaut. “High dynamic range imaging by pupil single-mode filtering and remapping”. *Monthly Notices of the Royal Astronomical Society* 373 (2006), 2 747–751.
- F. Roddier. “The effects of atmospheric turbulence in optical astronomy”. *Progress in optics* 19 (1981) 281–376.
- S. B. Shaklan. *Multiple beam correlation using single-mode fiber optics with application to interferometric imaging*. Ph.D. thesis, The University of Arizona. (1989).
- A. Sivaramakrishnan, D. Lafrenière, K. S. Ford, B. McKernan, A. Cheetham, A. Z. Greenbaum, P. G. Tuthill, J. P. Lloyd, et al. “Non-redundant aperture masking interferometry (AMI) and segment phasing with JWST-NIRISS”. In *SPIE Astronomical Telescopes+ Instrumentation*, 84422S–84422S (International Society for Optics and Photonics, 2012).
- A. Sivaramakrishnan, D. Lafrenière, P. G. Tuthill, M. J. Ireland, J. P. Lloyd, F. Martinache, R. B. Makidon, R. Soummer, et al. “Planetary system and star formation science with non-redundant masking on JWST”. In *SPIE Astronomical Telescopes and Instrumentation: Observational Frontiers of Astronomy for the New Decade*, 77313W–77313W (International Society for Optics and Photonics, 2010).
- J. Skilling and R. Bryan. “Maximum entropy image reconstruction-general algorithm”. *Monthly Notices of the Royal Astronomical Society* 211 (1984) 111.
- G. I. Taylor. “The spectrum of turbulence”. *Proceedings of the Royal Society of London Series A-Mathematical and Physical Sciences* 164 (1938), 919 476–490.
- P. Tuthill, S. Lacour, P. Amico, M. Ireland, B. Norris, P. Stewart, T. Evans, A. Kraus, et al. “Sparse aperture masking (SAM) at NAOS/CONICA on the VLT”. In *Proc. SPIE*, vol. 7735, 77351O–77351O (2010a).
- P. G. Tuthill. *Imaging stars through the atmosphere*. Ph.D. thesis, University of Cambridge (1994).
- P. G. Tuthill. “The unlikely rise of masking interferometry: leading the way with 19th century technology”. In *SPIE Astronomical Telescopes+ Instrumentation*, 844502–844502 (International Society for Optics and Photonics, 2012).
- P. G. Tuthill, N. Jovanovic, S. Lacour, A. Lehmann, M. Ams, G. Marshall, J. Lawrence, M. Withford, et al. “Photonic technologies for a pupil remapping interferometer”. In *SPIE Astronomical Telescopes and Instrumentation: Observational Frontiers of Astronomy for the New Decade*, 77341P–77341P (International Society for Optics and Photonics, 2010b).

- P. G. Tuthill, J. Lloyd, M. Ireland, F. Martinache, J. Monnier, H. Woodruff, T. ten Brummelaar, N. Turner, et al. “Sparse-aperture adaptive optics”. In *Astronomical Telescopes and Instrumentation*, 62723A–62723A (International Society for Optics and Photonics, 2006).
- P. G. Tuthill, J. D. Monnier, W. C. Danchi, E. H. Wishnow, and C. A. Haniff. “Michelson interferometry with the Keck I telescope”. Publications of the Astronomical Society of the Pacific 112 (2000), 770 555–565.
- J. Xiang. “Accurate compensation of the low-frequency components for the FFT-based turbulent phase screen”. Optics Express 20 (2012), 1 681–687.

## A. SAM Observing Guide

This guide teaches the user how to operate SAM on the student telescope at the Leiden Old Observatory. It discusses the pre-observing routine (involving all calibrations), note taking during observations and post-observing shutdown. This guide assumes that the user knows how to operate the telescope itself, and only discusses SAM procedures. It also assumes familiarity with SAM observations in general.

### A.1. Pre-observing

Before observing some calibrations need to be done:

1. Because of the filter design, in one night only two filters can be used, due to the design of the filter holder. The filter of the fast camera has to be changed manually. The camera and the long narrow tube of the beam expander can be unscrewed from the optical manifold to reveal two filters. Low and high-pass filters can be combined to form a bandpass filter. If only a single filter is used, an empty filter casing has to be added. After each filter, flatfields and detector orientation have to be recalibrated.
2. In the afternoon, the flatfield and dark frames need to be taken. Flatfields are taken without an aperture mask. Dark frames can be taken the usual way. Both need to be taken with the same settings that will be used in the observations of that night. Some of the important settings of `FireCapture` are the *gamma* (always at 100, which means linear detector response) and *gain* (as high as possible without saturating the detector).
3. The mask can be put on by sliding aside the four clips on the mask holder that hold the mask in place. The mask can be slid onto the holder and the clips put back on. Don't unscrew the clips completely, as these screw also hold the mask holder onto the telescope. If the mask has a shiny or bright side and a diffuse or dark side, the latter should be pointing into the telescope to avoid internal reflections.
4. At night the detector orientation can be calibrated. The telescope is brought out of focus such that all holes are visible in the image. The integration time can be large to reach the desired SNR.
5. The telescope can be pointed using the slow camera as a view finder. To find the position of the fast camera field of view on the CCD of the slow camera, the view finder can be used. Switching between instruments produces a small but insignificant change in pointing (< 5 arcsec).
6. Before each observation, the telescope needs to be focussed. This can be done in the usual way. Focussing with an aperture mask is a lot quicker than without one, provided that the telescope has been pointed at a bright object.

### A.2. During observing

During an observations several things need to be noted:

1. Care must be taken for telescope drift. The measurement must be stopped if the star is too close to the edge of the detector. The telescope can be realigned and the measurement restart. This takes about 10 minutes with the current pointing model.
2. The preview of **FireCapture** has to be turned off most of the time for reaching the highest fps (and therefore highest duty time). Sometimes the fps drops to unacceptable levels. A program restart solves this problem.
3. Important changes concerning vibrations of the telescope should be noted. This involves needed movement of the dome, opening and closing the dome door, etc.

### A.3. Post-observing

The mask should be removed after observations. The filters can be left in the filter holder.

## B. SAML Pipeline Manual

The pipeline was written in Python and is available from the corresponding author upon request<sup>5</sup>. It uses common numerical, scientific and plotting libraries: **Numpy**, **Scipy** and **Matplotlib**. The pipeline consists of a central library that carries out all the calculations and number crunching. This library consists of the following files:

- **avireader.py**. This file simplifies reading from an Audio Video Interleave file, which was the output of our observing program.
- **binaryfit.py**. This file fits a binary to the closure phase and handles contrast limits.
- **closurephases.py**. This file calculates the closure phases from visibilities and averages the closure phases over all frames.
- **datacutting.py**. This file is used to center the star and cut out a part of the image in which the star is centered. It can also window the data, for example with a super-Gaussian.
- **filters.py**. This file handles the loading of filters from files and provides certain standard filters.

---

<sup>5</sup>[por@strw.leidenuniv.nl](mailto:por@strw.leidenuniv.nl)

- `mask.py`. This file encapsulates the positions of the holes on the mask and can load it from a file. It provides the characteristics of the mask.
- `maskgen.py`. This file can generate mask according to the algorithms in Section 3.
- `psf.py`. This file implements the Discrete-Time Fourier Transform (DTFT) and provides functions for generating PSFs using a phase screen generator and/or an aperture.
- `seeingsim.py`. This file implements all algorithms discussed in Section 4.
- `snr.py`. This file provides simple calculations including SNR for stars in the V-band.
- `visibilities.py`. This file implements the fringe fitting and generates visibilities from an image file.

This library is used by the three main files of the pipeline. These files have to be run in order to reduce a dataset and mostly call functions from the core library after combining the measurements made by the user. These files are:

- `CalculateVisibilities.py`. This program reduces the raw observation data to a list of visibilities for each frame. It performs dark-correction, flatfielding and mask orientation calibration. This is done using the settings file `filenames.txt`, which includes the observation type, the used mask, the mask orientation, the used filter and the integration time for each observation file. This program is unaware of the type of object that is observed.
- `ClosurePhaseBootstrap.py`. This program reduced the visibilities into the closure phases for each target, used filter, used mask and mask orientation. It uses the user-defined settings file `targets.txt`. This file includes which targets were observed and which files belong to which target. Errors are determined using bootstrap and running this program multiple times sequentially will generate more bootstrap samples.
- `AnalysisClosurePhases.py`. This program analyses the closure phases and fits them to a binary, using the correct binary and calibrator. It combines the closure phases for different masks, mask orientations, and filters to use as much information as possible in a single fit. It uses the user-defined settings file `analysis.txt`, which includes which calibrator to use for which binary. This program uses bootstrap on the distribution of  $F$  under the null-hypothesis to calculate correct chi-squared maps and contrast limits. Again, running this program multiple times increases the number of bootstrap samples and therefore the accuracy of the data reduction.

The pipeline includes several other files, including `SimulationData.py` which can generate simulated data files using the phase screens discussed. These other files serve as sample code to the library. In the folders `Masks` and `Filters` the mask and filter files are located.